POLYPUBLIE
Polytechnique Montréal

Titre: Title:	Experimental Testing and Modelling of Variable Capacity Air-to-Air Heat Pumps
Auteur: Author:	Gregor Strugala
Date:	2020
Type:	Mémoire ou thèse / Dissertation or Thesis
Référence: Citation:	Strugala, G. (2020). Experimental Testing and Modelling of Variable Capacity Air-to-Air Heat Pumps [Master's thesis, Polytechnique Montréal]. PolyPublie. https://publications.polymtl.ca/5285/

Document en libre accès dans PolyPublie
Open Access document in PolyPublie

URL de PolyPublie: PolyPublie URL:	https://publications.polymtl.ca/5285/
Directeurs de recherche: Advisors:	Michaël Kummert
Programme: Program:	Génie énergétique

POLYTECHNIQUE MONTRÉAL

affiliée à l'Université de Montréal

Experimental testing and modelling of variable capacity air-to-air heat pumps

GREGOR STRUGALA

Département de génie mécanique

Mémoire présenté en vue de l'obtention du diplôme de *Maîtrise ès sciences appliquées*
Génie énergétique

Juin 2020

POLYTECHNIQUE MONTRÉAL

affiliée à l'Université de Montréal

Ce mémoire intitulé :

Experimental testing and modelling of variable capacity air-to-air heat pumps

présenté par **Gregor STRUGALA**
en vue de l'obtention du diplôme de *Maîtrise ès sciences appliquées*
a été dûment accepté par le jury d'examen constitué de :

Massimo CIMMINO, président
Michaël KUMMERT, membre et directeur de recherche
Justin TAMASAUSKAS, membre externe

ACKNOWLEDGEMENTS

RÉSUMÉ

La consommation énergétique des bâtiments représente une fraction importante de notre consommation énergétique globale et de nos émissions de gaz à effet de serre ; il devient donc essentiel d'améliorer leur efficacité. Les pompes à chaleur contribuent grandement à cet effort d'efficacité en diminuant significativement la consommation d'énergie de chauffage. Les pompes à chaleur de type air-air (qui utilisent l'air ambiant comme source de chaleur) sont assez populaires parce qu'elles ont un coût d'investissement sensiblement plus bas que les pompes à chaleur géothermiques. Elles sont cependant pénalisées par une efficacité et une capacité plus faibles lorsque la température ambiante est très basse, ce qui est particulièrement critique dans les climats froids. De plus, les pompes à chaleur à capacité fixe subissent une baisse d'efficacité provoquée par une opération intermittente.

Un type plus récent de pompe à chaleur équipée d'un compresseur à vitesse variable ne rencontre pas ces problèmes, mais leur coût d'investissement est toutefois plus élevé. La capacité variable introduit un niveau de complexité supplémentaire dans le design de systèmes de chauffage, ventilation et conditionnement d'air (CVCA), et il y a un manque de modèles dynamiques comparé à ce qui existe pour des capacités fixes. De plus, les données de performance fournies par les manufacturiers sont généralement incomplètes, ce qui rend encore plus difficile l'estimation des performances.

L'objectif de ce mémoire est de développer un modèle permettant d'intégrer ce type de machine dans des simulations d'installations CVCA. Ce modèle, développé dans le logiciel TRNSYS, se base sur des cartes de performance. Dans le but d'en établir une qui soit complète et précise, des tests expérimentaux ont été effectués au laboratoire de CanmetÉNERGIE à Varennes. Ces tests permettent aussi d'analyser et de modéliser les stratégies de contrôle de la machine.

Les tests montrent que la capacité en chauffage indiquée dans les données du manufacturier est un petit peu surestimée à basse température, mais elle correspond assez bien aux mesures au-delà de $-10\,°C$. Les valeurs de capacité en climatisation semblent avoir une corrélation moindre avec la température extérieure, mais des tendances similaires sont néanmoins observées. Le coefficient de performance semble quant à lui correspondre assez bien aux mesures, ce qui permet d'utiliser avec confiance ces données dans le modèle.

Des régressions sont déduites des résultats expérimentaux afin de pouvoir extrapoler la carte de performance aux conditions qui ne sont pas couvertes. Elles permettront aux utilisateurs du modèle d'établir une carte de performance complète, même sans effectuer de tests.

Finalement, les résultats de simulations reproduisant l'environnement expérimental présentent un comportement généralement similaire à ce que l'on observe dans les tests, avec toutefois quelques disparités. En effet, certains comportements particuliers de la machine testée ne sont pas repris dans le modèle. Cela permet d'avoir un modèle générique, paramétrable à partir des données typiquement fournies par les manufacturiers. Une étude de cas montre une utilisation du modèle dans une application réaliste à une unité de logement dans le climat de Montréal. Les principaux mécanismes de contrôle implémentés sont mis en évidence en discutant des résultats pour des jours spécifiques.

ABSTRACT

Since decarbonizing the electricity grid and reducing society's energy consumption is becoming paramount, it is essential to improve the energy efficiency of the building sector, which accounts for an important part of the global energy consumption.

Air-to-air heat pumps (which exchange energy between indoor and ambient air) allow to heat or cool a space with greater efficiency than traditional heating systems, which makes them a key component in improving energy efficiency. They are often preferred to ground source systems because of their lower investment cost; however, they have limitations. Their operating temperature range is limited and their capacity and efficiency decrease at low ambient temperatures, which can be a problem in cold climates. Moreover, most existing heat pumps operate by alternating between *on* and *off* modes (i.e. they cycle), which has the side effect of lowering their performance. Variable capacity heat pumps tackle these problems by using variable speed compressors to adjust their capacity as needed, thereby removing the need for cycling. Thus, they can reach higher energy efficiencies, but also have higher investment costs. Variable capacity air-to-air heat pumps (VCAAHPs) are gaining in popularity, especially in cold climates where they can sustain wider temperature ranges.

As opposed to fixed capacity heat pumps, VCAAHPs lack simulation models, making it difficult to integrate them into simulations of HVAC systems. Manufacturers provide performance data, but they are severely incomplete, and not always accurate. Therefore, there is a clear need for a VCAAHP model and a more complete performance map.

The main goal of the thesis is therefore to develop a VCAAHPs model to use in simulations of HVAC systems. Developed as a component for the TRNSYS software, the model uses the "black box" approach and relies on performance maps. To build a complete performance map that could actually be used by the model, experimental tests were conducted at the CanmetENERGY laboratory in Varennes, Québec. Apart from the performance data, these tests are also useful in establishing the control strategies of the heat pump, which play an important role in the model as well.

Test results show that heating capacity stated by manufacturer is slightly overestimated at low temperatures, but it matches well the measurements above $-10\,°\mathrm{C}$. Capacity and outdoor temperature values appear to be less correlated in cooling mode, yet similar trends are still observed. The coefficient of performance (COP) values given by the manufacturer seem to match the measurements quite well, which gives confidence to the data used in the model.

Regressions are developed from experimental results to obtain performance values for conditions that are not covered by the initial performance map. They allow users to build a complete performance map even without performing tests.

Finally, simulations results reproducing the testing environment show a similar behaviour to what is observed in experiments, with some discrepancies. Some behaviours specific to the tested machine were not considered in the model. This makes the model more generic and parametrizable, using data typically provided by manufacturers. Model usage is demonstrated through a case study modelling a residential unit in the Montréal climate. Various implemented behaviours are highlighted by showing results of specific days.

TABLE OF CONTENTS

LIST OF TABLES

LIST OF FIGURES

LIST OF SYMBOLS AND ACRONYMS

COP	Coefficient of performance
COP_h	COP in heating mode
COP_c	COP in cooling mode
ΔT_r	Return air wet-bulb depression
e	Error signal of the heat pump controller
e_min	Error signal lower limit
e_max	Error signal upper limit
f_c	Compressor frequency
$\hat{f}_c$	Unsaturated compressor frequency
f_0	Minimum compressor frequency
$\tilde{f}$	Maximum compressor frequency
f_1	Maximum compressor frequency for long operation
f_2	Boost frequency
γ	Heat pump operating mode
GHG	Greenhouse gas
H_i	Enthalpy of the refrigerant at point i
h_i	Specific enthalpy of the refrigerant at point i
HVAC	Heating, ventilation and air conditioning
k_p	Controller proportional constant
$\dot{m}_\text{r}$	Refrigerant mass flow rate
$\dot{m}_\text{a}$	Indoor unit air mass flow rate
ν	Normalized frequency

φ_{c1}	Cooling capacity correction by frequency
φ_{c2}	Input power correction by frequency in cooling mode
φ_{h1}	Heating capacity correction by frequency
φ_{h2}	Input power correction by frequency in cooling mode
ϕ_{oa}	Outdoor air relative humidity
ϕ_r	Indoor return air relative humidity
ϕ_s	Indoor supply air relative humidity
P_{comp}	Compressor power input
P_{el}	Total electrical power input
P_{fi}	Indoor unit fan power input
P_{fo}	Outdoor unit fan power input
p_i	Pressure of the refrigerant at point i
p_r	Indoor return air pressure
p_s	Indoor supply air pressure
PLR	Part load ratio
$\dot{Q}$	Heat pump capacity—either in heating or cooling mode
$\dot{Q}_{abs}$	Heat absorption rate in heating mode
$\dot{Q}_c$	Cooling capacity
$\dot{Q}_{co}$	Heat transfer rate at the condenser
$\dot{Q}_{ev}$	Heat transfer rate at the evaporator
$\dot{Q}_h$	Heating capacity
$\dot{Q}_{l,co}$	Refrigerant heat loss rate between the condenser and the compressor
$\dot{Q}_{l,co}$	Refrigerant heat loss rate between the evaporator and the compressor
$\dot{Q}_{rej}$	Heat rejection rate in cooling mode

s^{-1}	Integration operator (s being the Laplace variable)
s_i	Entropy of the refrigerant at point i
SHR	Sensible heat ratio
$\hat{t}$	Time since the end of last defrost, normalized by τ_{rec}
T_{amb}	Ambient temperature
T_o	Outdoor air temperature
T_r	Indoor return air dry-bulb temperature
T_s	Indoor supply air dry-bulb temperature
$T_{\mathrm{wb}o}$	Outdoor air wet-bulb temperature
$T_{\mathrm{wb}r}$	Indoor return air wet-bulb temperature
τ_{df}	Defrost duration
τ_{h}	Heating operation duration during a defrost cycle
τ_i	Controller integral time constant
τ_{rec}	Recovery mode duration after defrost
τ_{ss}	Steady-state mode duration after recovery
τ_t	Tracking time constant for the anti windup
U	Internal energy of the refrigerant
$\dot{V}_a$	Indoor unit air volumetric flow rate
VCAAHP	Variable capacity air-to-air heat pump
W	Compressor work on the refrigerant
ω_{oa}	Outdoor air humidity ratio
ω_r	Indoor return air humidity ratio
ω_s	Indoor supply air humidity ratio

LIST OF APPENDICES

CHAPTER 1 INTRODUCTION

In a context where decreasing our energy consumption and greenhouse gas emissions is becoming a top priority, heat pumps are expected to play a key role in improving the energy efficiency and decreasing the carbon footprint of the building sector. Their main application is space heating and cooling, which account for a large fraction of buildings energy consumption in most industrialized countries. For example, Natural Resources Canada estimates that fraction to be about 63 % of the energy consumed in the residential sector [1].

Variable capacity heat pumps can be even more efficient than typical fixed capacity heat pumps because they can vary the speed of their compressor. Moreover, their components can be oversized to reach a wider operating temperature range without lowering their performance, which is particularly useful in regions with very different climate conditions during the year, such as in Canada. Naturally, variable capacity air-to-air heat pumps (VCAAHPs) are gaining popularity in North America, due to their low investment cost. However, despite this, there is a lack of models that can adequately predict their performance and simplify their integration in the design of HVAC systems. Manufacturer data can be used, but they are not easy to integrate into simulations and are often incomplete and imprecise, making them unreliable [2]. In this thesis, the approach to overcome these problems is to create a dynamic TRNSYS model[1] relying on performance maps and perform experimental testing to build a complete and reliable performance map.

1.1 Definitions and basic concepts

Heat pumps transfer heat between two different reservoirs of water or room air using a process called *refrigeration*. This process consists in transferring heat from a region to another warmer one—with the same direction as the temperature gradient—as opposed to a spontaneous heat transfer, according to Fourier's law. The terms *cold source* and *hot source* usually denote the lower and higher temperature region respectively. The useful effect of a heat pump can be to reject heat to the hot source or absorb heat from the cold source. The heat pump then respectively operates in *heating* or *cooling* mode.

To maintain comfortable conditions in a building, heat is thus supplied in heating mode and extracted in cooling mode. In either case, the corresponding heat transfer rate is referred to as the *capacity* of the heat pump. A terminology difference is made between the capacity

---

[1]TRNSYS is a software environment used to simulate the behaviour of transient systems.

in heating mode, called *heating capacity* and noted $\dot{Q}_\mathrm{h}$, and the capacity in cooling mode, called *cooling capacity* and noted $\dot{Q}_\mathrm{c}$.[2]

Heat transfer in heat pumps is usually achieved by changing the phase of a substance called the *refrigerant*. On the cold source side, heat is absorbed by evaporating the refrigerant, and then rejected on the hot source side by condensing it (fig. 1.1). Doing so at different temperatures requires some work on the refrigerant to raise its pressure—that is, to compress it. The refrigeration cycle therefore needs a work input W in cooling as well as in heating mode (fig. 1.2). The heat pumps studied in this project are of the air-to-air type, meaning that the building and the environment mentioned in fig. 1.2 are the indoor and outdoor air, respectively.
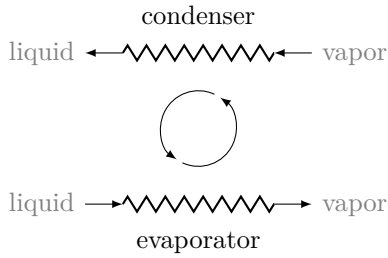
Figure 1.1: Phase changes are performed by passing the refrigerant through heat exchangers called the evaporator and condenser. The refrigerant is kept in a closed loop and goes through a series of transformations referred to as the *refrigeration cycle*.
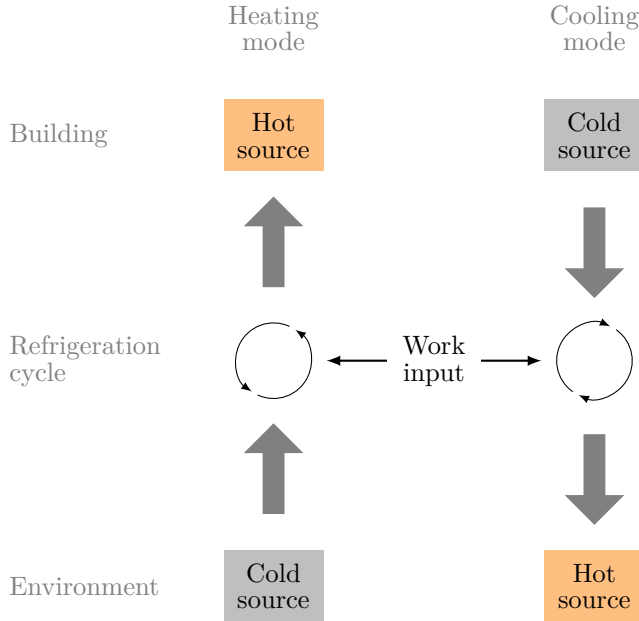
Figure 1.2: The building can either be the hot or cold source, depending on the operation mode. Changing the operation mode also reverts the direction of the refrigeration cycle and heat transfers: the evaporator becomes the condenser and the condenser becomes the evaporator.

The building side usually corresponds to the indoor air or domestic water, and the environment is generally the outdoor air or another fluid exchanging heat.

The heat transfer rate occurring at the condenser is not exactly equal to the heating capacity, because auxiliary elements—typically fans to apply forced convection—also produce heat.

---

[2]By convention, all quantities having dimensions of power or energy are taken as positive, and their actual sign is deduced from the context.

This is also true for the evaporator, where air condensation can also influence the capacity. For this reason, heat transfer rates at the condenser and evaporator are noted $\dot{Q}_{co}$ and $\dot{Q}_{ev}$ respectively, to distinguish them from $\dot{Q}_h$ and $\dot{Q}_c$.

The refrigerant goes through a loop; hence, it has no internal energy variation over a cycle in steady-state: $\oint dU = 0$. Assuming that the only energy changes are caused by the work input, the heat transfer in the exchangers, and the heat losses between the work input and the exchangers, the energy balance on the refrigerant can therefore be written as

$$\oint dU = W + Q_{ev} + Q_{l,ev} - Q_{co} - Q_{l,co} = 0$$

and, by derivating with respect to time:

$$\dot{W} + \dot{Q}_{ev} + \dot{Q}_{l,ev} = \dot{Q}_{co} + \dot{Q}_{l,co} \tag{1.1}$$

The most frequently used refrigeration cycle is the *vapor-compression refrigeration cycle*, depicted in fig. 1.3. In this type of cycle, the work input is provided by a compressor that raises the pressure of the refrigerant while it is in vapour state. An isenthalpic valve expands the refrigerant after it has been condensed to allow evaporation at a lower temperature level. The heat transfers at the exchangers and the compressor work input are given by the enthalpy differences at the inlet and outlet. In heating mode for example,

$$W = H_2 - H_1$$
$$Q_{ev} = H_6 - H_5$$
$$Q_{co} = H_3 - H_4$$
$$Q_{l,ev} = H_1 - H_6$$
$$Q_{l,co} = H_2 - H_3$$

Given a refrigerant mass flow rate $\dot{m}_r$, the power input and heat transfer rates become

$$\dot{W} = \dot{m}_r(h_2 - h_1)$$
$$\dot{Q}_{ev} = \dot{m}_r(h_6 - h_5)$$
$$\dot{Q}_{co} = \dot{m}_r(h_3 - h_4) \tag{1.2}$$
$$\dot{Q}_{l,ev} = \dot{m}_r(h_1 - h_6)$$
$$\dot{Q}_{l,co} = \dot{m}_r(h_2 - h_3)$$

The transformation $4 \to 5$ being isenthalpic, eqs. (1.2) are coherent with eq. (1.1). This can

be directly seen in *p-h* diagrams of fig. 1.3.
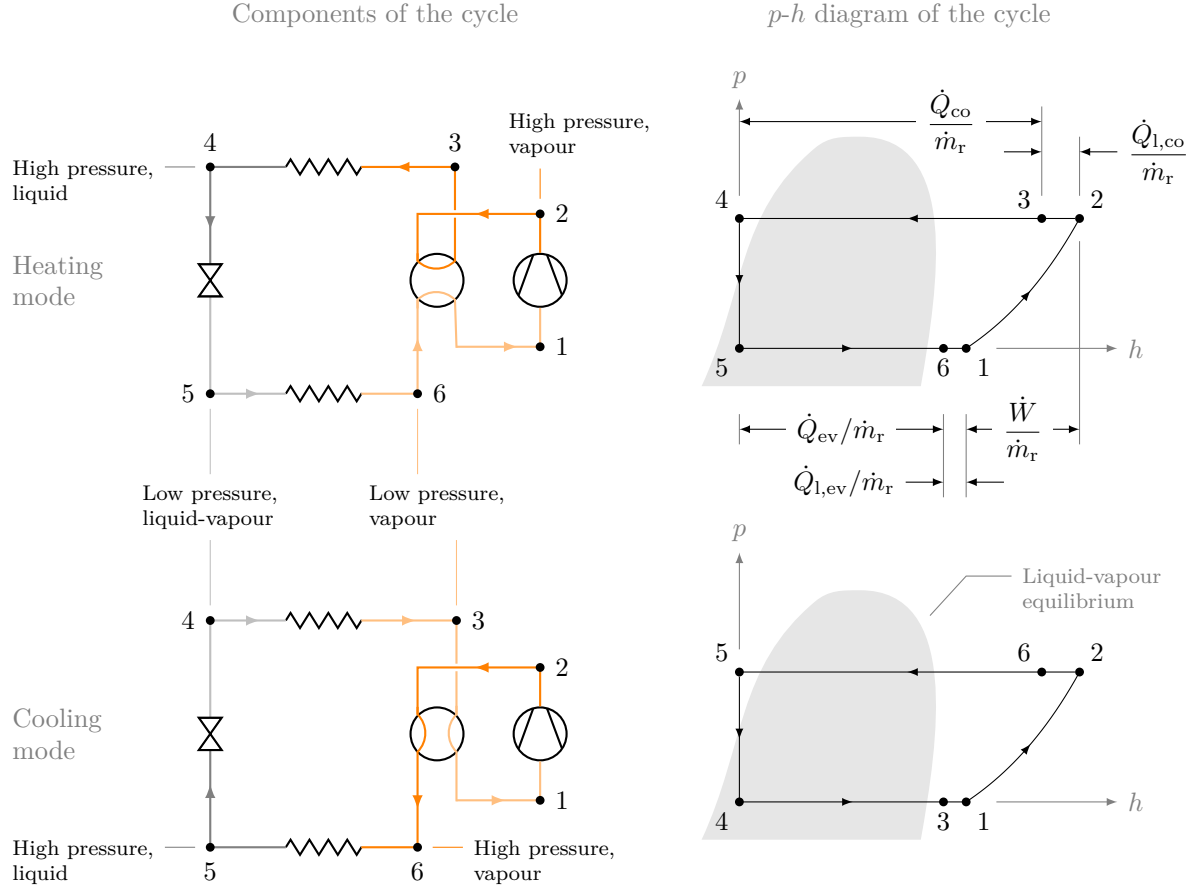
Figure 1.3: Basic refrigeration cycle in heating and cooling modes.

Performance is evaluated by comparing the heat pump capacity—the "useful" effect—to the power input. The COP, defined as the ratio between those two quantities, gives a quantitative description of a heat pump's performance. Since the heat pump capacity is different in heating and in cooling, the COP also depends on the operating mode:

$$\mathrm{COP_h} = \frac{\dot{Q}_\mathrm{h}}{\dot{W}}$$

$$\mathrm{COP_c} = \frac{\dot{Q}_\mathrm{c}}{\dot{W}}$$

Global performance over a given time period is evaluated by integrating the capacity and power input over that period. As explained in the next section, the global COP of fixed capacity heat pumps over an extended period is lower than their COP at rated conditions. Increasing this global COP is, in essence, the purpose of variable capacity.

1.2 Relevance

Variable capacity heat pumps studied in this thesis are equipped with an inverter-driven compressor able to vary its speed. By adjusting the frequency of the compressor, the capacity can be adapted to keep the room temperature around a given value, whereas fixed-capacity heat pumps have to switch on and off to do so. The specific capacity required to achieve a desired room temperature is called the *load* and is depicted by black lines in fig. 1.4. Besides a reduction of temperature oscillations that improves thermal comfort, variable capacity heat pumps have two main advantages: a higher performance and a wider temperature range.

Figure 1.4: A fixed capacity heat pump must adjust the time during which it is turned on to adapt to a change in the load. On the other hand, a variable capacity heat pump can set its capacity to be exactly equal to the load.

Since most heat demands are not constant over time, any fixed-capacity system will have to turn on and off to balance the load and keep a (more or less) constant temperature level. When a heat pump turns on, it goes through a transient regime during which the capacity increases slowly until a steady-state is reached. Because the input power level stays approximatively the same, this transition causes a performance degradation. However this degradation becomes less significant as the heat pump keeps operating in steady-state, since the heat "lost" during the transient period becomes smaller compared to the total heat provided (fig. 1.5).

The time duration during which a heat pump is turned on to balance the load, τ_{on}, depends on the acceptable temperature limits, and the relative difference between the capacity $\dot{Q}$ and the load,

$$\frac{\dot{Q} - \dot{Q}_{\mathrm{load}}}{\dot{Q}} = 1 - \frac{\dot{Q}_{\mathrm{load}}}{\dot{Q}}$$

where the ratio $\dot{Q}_{\mathrm{load}}/\dot{Q}$ is called the *part load ratio* (PLR). When $\dot{Q}_{\mathrm{load}} \geq \dot{Q}$, the heat pump operates at full load whatever the value of $\dot{Q}_{\mathrm{load}}$ is, so the actual definition of the PLR is

$$\mathrm{PLR} = \min\left(1, \frac{\dot{Q}_{\mathrm{load}}}{\dot{Q}}\right)$$

When the PLR increases, so does τ_{on} (fig. 1.6) and thus also the COP. The goal of variable

(a) The steady-state time is the same as the transient time.

(b) The steady-state time is five times longer than the transient time.
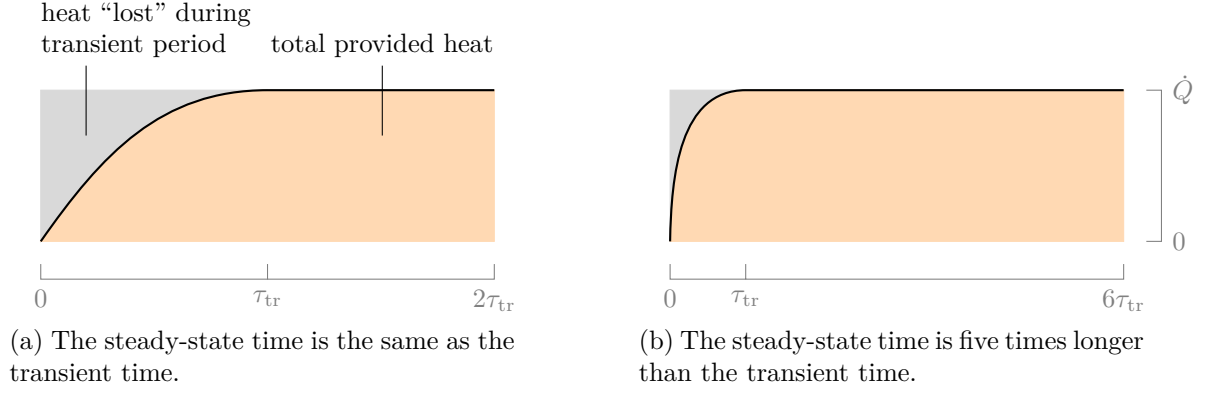
Figure 1.5: The fraction of lost heat becomes smaller as the steady-state time gets larger compared to the transient time.

capacity heat pumps is to keep the PLR close to 1 by reducing the cycling, thereby improving the global performance.
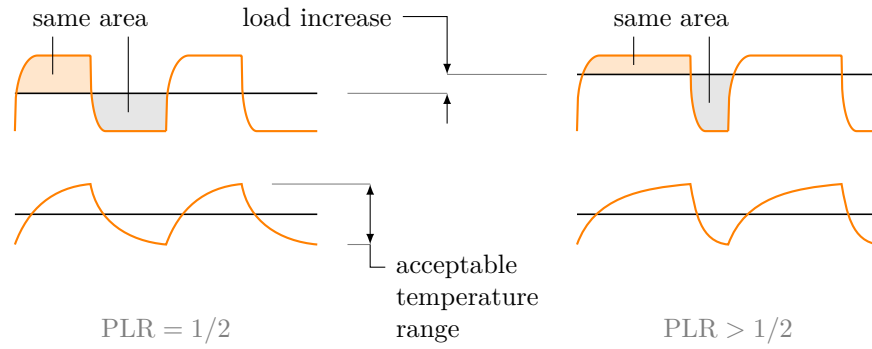
Figure 1.6: The time during which a heat pump is turned on increases with the PLR.

Another advantage of having a variable capacity is an increased operating temperature range. Because the heating capacity decreases with the outdoor temperature, fixed capacity heat pumps require an auxiliary, less efficient heating supply below a certain ambient temperature (called the thermal balance point) to balance the load. Oversizing the heat pump to have a higher capacity is not an efficient solution, since this would result in excessive cycling frequency [3], as illustrated in fig. 1.7. In contrast, the capacity of variable capacity heat pumps can be set high enough to work at lower temperatures and then decreased at mild outdoor temperatures (when $T_{\text{eq}} < T_{\text{o}} < T_{\text{set}}$).

As it stands now, modelling such variable capacity devices proves difficult, for there is a lack of dynamic models able to predict accurately their behaviour and performance in a user-friendly way. In addition, using performance data from manufacturers in a simulation can

Figure 1.7: The cycling frequency increases with the capacity because the difference between the capacity and the load increases too.
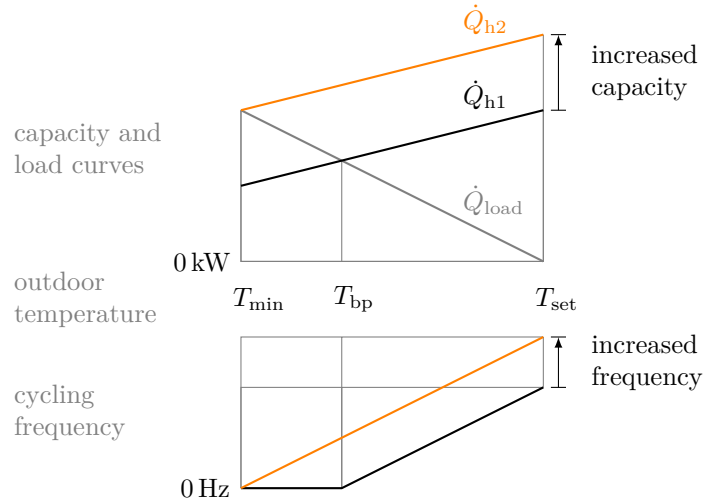
be very tedious and require much more work than it should. There is thus a clear need for an adequate model.

There is another caveat when using manufacturer data: it is often found to be incomplete and not really accurate, which makes it unreliable. Appendix B shows a typical example of how performance maps are provided by manufacturers. Chapter 4 details what *should* be found in a performance map, but it can already be seen that some crucial information is missing, such as the frequency (no values provided) or the air flow rate dependency (only one value provided). Moreover, the manufacturer data can sometimes be quite different from measured values, as shown by Kegel et al. [4]. Because the performance map has a major impact on the model accuracy, it needs to be complete; hence new experimental data is required for the model to work properly.

Of course, the experimental results are potentially not going to be the same for different heat pumps. However, someone using the model will usually not have access to such experimental data; the only alternative is using the data provided by the manufacturer. Although it is not ideal, this approach could be improved by using the test results, e.g., by developing regressions, to extrapolate the manufacturer data and fill its missing values. The result would be a hybrid between a performance map approach, and a polynomial function approach such as the one used in the EnergyPlus system curve based model of variable refrigerant flow heat pump [5, section 16.7.1]. Unfortunately, the EnergyPlus model apparently does not have a frequency correction, which is a key quantity for variable speed devices. To make this process easier, a methodology should guide the user who wishes to complete the performance map of the heat pump to be simulated. This kind of work usually being tedious, parts of the process should also be automated to improve the user experience.

1.3 Research objectives

The main goal of this thesis is to increase the body of knowledge on VCAAHP performance and to provide detailed simulation tools to design systems incorporating this technology. Four specific objectives are defined:

1. determine the control strategies of a real heat pump from experimental test results and manufacturer information;

2. build a complete and accurate experimental performance map for this same heat pump;

3. implement a TRNSYS model relying on performance maps to simulate VCAAHPs in heating and in cooling mode; and

4. establish a methodology to complete performance data provided by manufacturers based on regressions from experimental results.

1.4 Thesis outline

The context, the need and the objectives were presented in this chapter, along with the global part of the literature review. The specific elements are distributed in each relevant chapter.

The second chapter shows an overview of the test bench and defines the main quantities that are useful in the following chapters.

The third chapter focuses on determining the control strategies and how the heat pump operates, by comparing the information from the manufacturer and the experimental results.

A method to reach the objectives 2 and 4 is presented in the fourth chapter. Steady-state experimental results are discussed to draw conclusions on how to build the performance map. Regressions to extrapolate typical manufacturer performance maps are established.

The fifth chapter details the requirements of the model, its different components and how they work together. Some simulations results are then presented and discussed.

Finally, global conclusions are given with recommendations for future work.

CHAPTER 2   TEST BENCH

The objective of the test bench is threefold. First, it imposes a set of environmental conditions to the heat pump, corresponding to a particular performance map entry. Second, it sets the frequency of the heat pump by varying the load. And third, it measures the power input and the capacity corresponding to the imposed conditions. This chapter details the test bench components and the relevant quantities to be measured. Measured quantities consist of, on the one hand, the quantities actually included in the environmental conditions, i.e. that have an impact on the performance, and on the other hand, the power input and the quantities required to compute the heat pump capacity.

The environmental quantities impacting the performance obviously include the source and sink temperatures and air flow rates, which affect the heat transfer. Since the outdoor unit fan speed is not varying, the outdoor air flow rate is not included in the inputs. Another quantity to consider is the humidity. In heating mode, it affects the frequency and duration of defrost cycles, and in cooling mode, it affects the latent load. Those four quantities (indoor return temperature and humidity, outdoor temperature, and indoor air flow rate) constitute, along with the compressor frequency, the input variables of the performance maps. The frequency is not strictly speaking a model input, because it is adjusted internally from the return air and setpoint temperatures.

The environmental test chamber is composed of two sheds (fig. 2.1a), in which the temperature or the load is controlled by a fan bringing ambient air from outside and an auxiliary heater. The fresh air flow rate and auxiliary heater are controlled to meet desired test conditions. The fan of the indoor shed (fig. 2.1b) is used to impose a load—which should be equal to the capacity in steady-state—that the heat pump must compensate to maintain the return temperature at $T_r = T_{\text{set}}$. The capacity and thus also the frequency level can be adjusted by varying the load. The setpoint T_{set} is specified directly to the heat pump. In cooling mode, the return air humidity must be controlled since it is part of the performance map input quantities. The test bench is not equipped to actually humidify the air, but the fan can be used to regulate the humidity instead of the load and the electrical heater can be used for load control. In the outdoor shed, the fan is used to control the "tested" outdoor temperature T_o (as opposed to the actual ambient temperature outside of the shed T_{amb}) instead of the load. In cooling mode, in case T_{amb} is smaller than the desired value for T_o, the auxiliary heater can be used to further increase the temperature. The outdoor air humidity is also measured, as it is an entry of the heating performance map.

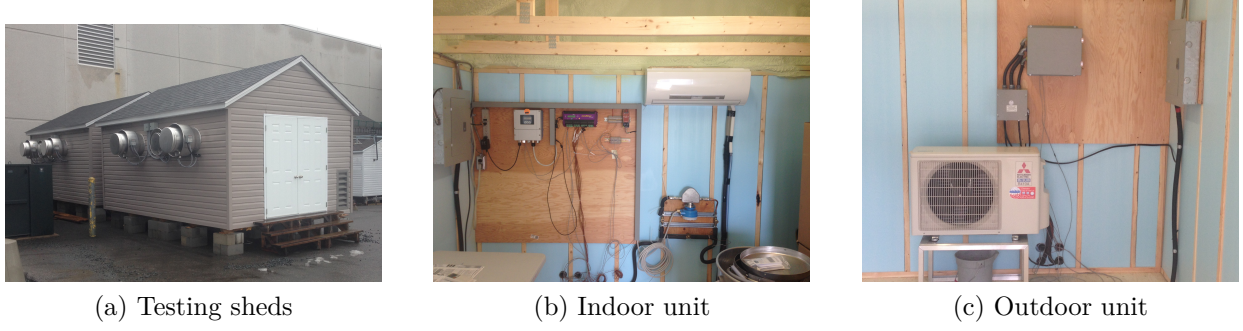(a) Testing sheds   (b) Indoor unit   (c) Outdoor unit

Figure 2.1: A test bench with a mini-split variable capacity heat pump was set up at Natural Resources Canada, CanmetENERGY in Varennes.

Temperature, humidity and power sensors are depicted in fig. 2.2. The state of point s is necessary in cooling mode in order to compute the sensible and latent heat fractions.

There are two ways to obtain the value of the capacity: from the measurements on the return and supply air from the measurements on the refrigerant. In heating mode, the heat transfer rate from the condenser to the air is $\dot{Q}_{co} = \dot{m}_r(h_3 - h_4)$. Assuming that the energy input of the fan P_{fi} is entirely converted to heat, the heating capacity is given by $\dot{Q}_h = \dot{m}_r(h_3 - h_4) + P_{fi}$. On the air side, $\dot{Q}_h = \dot{m}_a(h_s - h_r)$. In cooling mode, the heat transfer rate from the air to the evaporator is $\dot{Q}_{ev} = \dot{m}_r(h_4 - h_3)$. Contrary to heating mode, the state 4 is *after* the expansion valve, which means that it corresponds to a saturated liquid-vapour mixture. Since there is no way to actually know the refrigerant quality in this state, its enthalpy is unknown as well. Therefore, the expansion valve is assumed to be totally isenthalpic, so that $h_5 \approx h_4$ can be used instead, as the refrigerant in state 5 is a subcooled liquid (see fig. 1.3). As for heating mode, the air is heated by the fan, but it may also lose heat from condensation. Accordingly, the cooling capacity is $\dot{Q}_c = \dot{m}_r(h_4 - h_3) - P_{fi} + \dot{m}_w h_w$. Since the condensate mass flow rate is very small and excessively hard to measure dynamically, its influence is neglected. On the air side, $\dot{Q}_c = \dot{m}_a(h_r - h_s)$.

The sensible and latent heat absorption rate from the heat pump can only be determined from air measurements. Their computation requires the use of an intermediate state enthalpy $h_x = h(T_r, \omega_s)$, as does the model when it computes the supply air state (fig. 5.6). They are then given by $\dot{Q}_{cs} = \dot{m}_a(h_x - h_s)$ and $\dot{Q}_{cl} = \dot{m}_a(h_r - h_x)$.

The enthalpies involved in the capacity calculations are obtained from the measurements of fig. 2.1, using the CoolProp library [6]. For the refrigerant enthalpies, only two pressure levels (p_1 and p_2) are used, i.e. the pressure drops in the refrigerant lines are neglected, as in fig. 2.1. For the enthalpies of the return and supply air, an atmospheric pressure of 1 atm is assumed—the fan pressure drop is neglected, since $\frac{p_r - p_s}{p_r} \ll 1$.
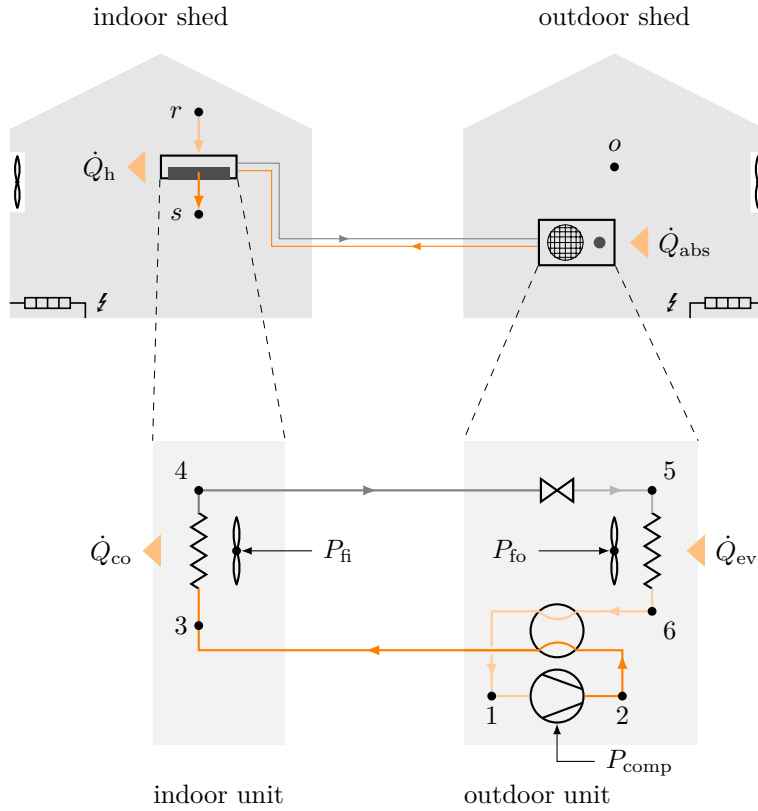
Figure 2.2: Diagram of the test bench, in heating mode configuration. The dry bulb temperature and relative humidity are measured at points r, s and o. The refrigerant temperature is measured at points $1 \rightarrow 6$ and its pressure at points 1 and 2. The three power inputs P_{comp}, P_{fi} and P_{fo} are measured as well.
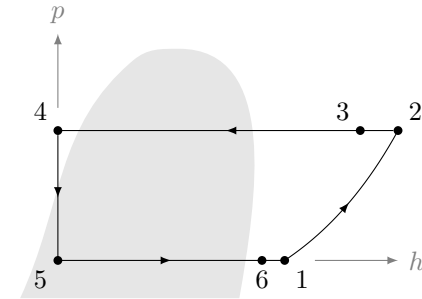
The air flow rate in the indoor unit is more difficult to measure than the other quantities. Being distributed over a large area, it has to be concentrated with a converging plenum to a region small enough that the velocity distribution can be assumed to be uniform. However, encasing the indoor unit with a plenum causes a pressure drop. Since the fan operates at a low power level, this pressure drop is enough to decrease the flow rate significantly, which causes the measured value to be smaller than the flow rate in normal operating conditions. The pressure drops thus needs to be compensated; one way to do so is to use a *duct blaster* (see fig. 2.3). By using an additional fan to balance the pressure drop, the air flow rate associated with each setting of the fan speed (*high*, *medium*, *low* and *quiet*) can be measured without being altered by the plenum. The measured values are presented and compared to manufacturer values in table 3.1 (page 21).

Among the two ways of computing the heat pump capacity, the method based on air measurements is found to be less accurate, essentially because the air flow rate $\dot{m}_{\text{a}}$ is hard to measure precisely, whereas measurements of the refrigerant mass flow rate, obtained with a coriolis flow meter, are much more precise—with an uncertainty of only $\pm 0.2\,\%$, and $\pm 1.5\,\%$ when $\dot{m}_{\text{r}}$ is below $25\,\%$ of the rated value [7]. Moreover, the supply temperature and humidity sensors are located at the indoor unit outlet, where the air flow rate has a really non-uniform distribution and undergoes a lot of fluctuations. Using the refrigerant measurements is thus
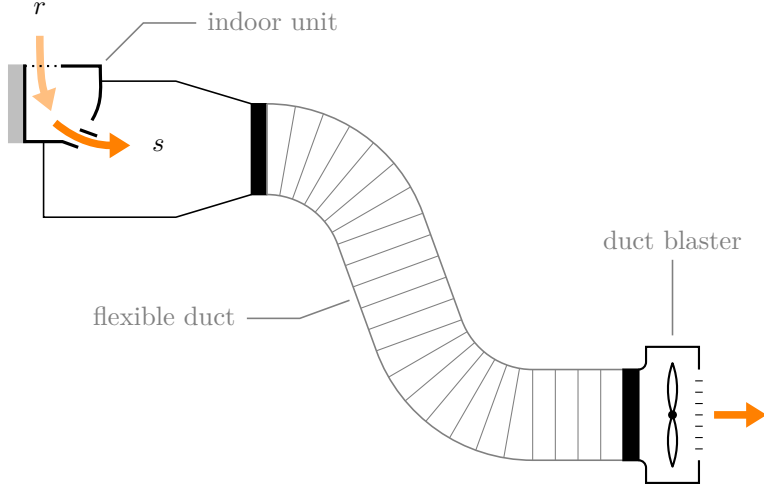
Figure 2.3: By varying the speed of the fan, the duct blaster is able to balance the pressure drop caused by the plenum surrounding the indoor unit outlet. Based on the fan speed and pressure measurements in the plenum and the fan housing, the device can then deduce the air flow rate.

preferred, and air side measurements are kept for validation.

Refrigerant measurements on their own are not sufficient to determine the sensible and latent capacities. However, they can be used to avoid resorting to the air mass flow rate as in the method presented above. Indeed, the sensible heat ratio (SHR), defined as the ratio $\dot{Q}_{cs}/\dot{Q}_c$, can be computed from the air enthalpies (see fig. 2.4)

$$\text{SHR} = \frac{\dot{m}_a(h_x - h_s)}{\dot{m}_a(h_r - h_s)} = \frac{h_x - h_s}{h_r - h_s} \tag{2.1}$$

Combined with the total capacity $\dot{Q}_c$ computed on the refrigerant side, $\dot{Q}_{cs} = \dot{Q}_c \, \text{SHR}$ and $\dot{Q}_{cl} = \dot{Q}_c \, (1 - \text{SHR})$.
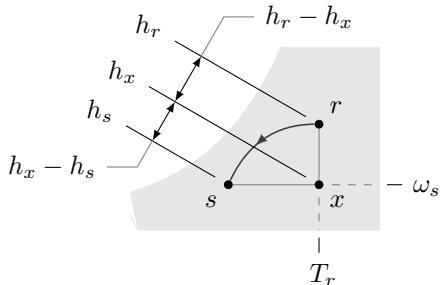
Figure 2.4: When there is latent heat, the supply air state is determined through an intermediate state x.

CHAPTER 3   CONTROL

Establishing the control strategies of a heat pump is not that easy, for manufacturers provide little information about them, and they are hard to guess from experimental results. Nonetheless, both the manufacturer instruction manuals and test results can bring some insights, especially concerning the operating ranges. Standard control strategies can be used instead when information is missing.

The primary objective of the controller is to keep the room temperature T_r around a given setpoint T_{set}. To do so, it controls four intermediate variables influencing the value of T_r. Those four control variables are

1. the compressor frequency, setting the power input,

2. the operating mode, which determines whether the air is heated or cooled,

3. the fan speed mode, which dictates the indoor unit air flow rate value,

4. the defrost mode, which decides the duration and frequency of defrost cycles.

3.1   Compressor frequency control

According to the manufacturer service instruction manual [8], the tested heat pump's frequency depends on the indoor return temperature (or more precisely, on the *error signal*), the outdoor temperature and, in cooling mode, the air mass flow rate. The error signal is defined as $e \triangleq T_{\mathrm{set}} - T_r$; the compressor frequency is actually modulated only when $e \in [e_{\min}, e_{\max}]$. In heating mode, the frequency is zero when $e < e_{\min}$ and set to its maximum value when $e > e_{\max}$, and it is the opposite in cooling mode. For the tested heat pump, $e_{\min} = -2.5\,°\mathrm{C}$ and $e_{\max} = 3\,°\mathrm{C}$ in heating mode. In cooling mode, $e_{\min} = -2\,°\mathrm{C}$ and $e_{\max} = 2.5\,°\mathrm{C}$. When $e \in [e_{\min}, e_{\max}]$, the frequency is modulated between a minimum and a maximum value that can vary depending on the environmental conditions. This dependence is detailed in section 3.1.2.

3.1.1   Normal operation

Although the service instruction manual provides much information about special operating modes, nothing is said of the frequency control during normal operation, when the signal error and the compressor frequency vary within their limits. Since it is common for heating

and cooling thermostats to use PI control [9], this same strategy will be assumed here. The PI controller depicted in fig. 3.1 can be tuned through its proportional and integral constants, respectively k_p and k_p/τ_i.
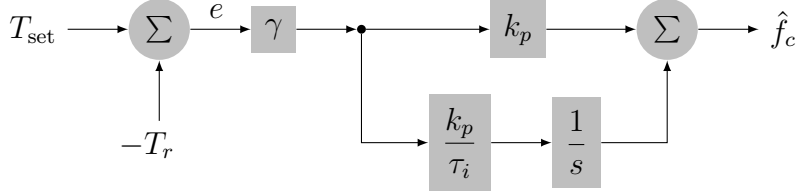
Figure 3.1: The unsaturated frequency $\hat{f}_c$ is computed using a PI controller. The parameter $\gamma = 1$ in heating mode and -1 in cooling mode, since in cooling mode the error sign needs to be reversed.

3.1.2 Frequency saturation

To avoid damages in the system, the compressor frequency is limited by the controller. The frequency limits are usually not constant and depend on environmental conditions. To ensure that the frequency stays within its limits, the unsaturated frequency $\hat{f}_c$ goes through a saturation block (see fig. 3.2).

Figure 3.2: The saturated frequency is bounded by a minimum frequency f_0 and a maximum frequency $\tilde{f}$: $f_{c,\text{sat}} = \min(\tilde{f}, \max(f_0, \hat{f}_c))$.

In heating mode, the minium frequency is a function of the outdoor temperature (fig. 3.3a), and the maximum frequency is constant: $\tilde{f} = 119\,\text{Hz}$.

When operating in cooling mode, the compressor—located in the outdoor unit—is exposed to high temperatures that could cause damage. As the heat rejection increases with the capacity and thus the frequency, there must be an upper frequency limit to prevent the compressor from heating too much. This upper limit depends on two quantities: there is obviously the outdoor temperature, but also the indoor air flow rate. Increasing the air flow rate decreases the frequency required to balance the load, and the heat rejection with it. This means that the upper frequency limit can be higher.

In order to reach the setpoint faster at startup, there are two different frequency limits. In addition to the steady-state limit f_1, there is a transient, slightly higher limit f_2 (referred to

as the *boost frequency*) at which the controller can operate for a maximum duration of 30 minutes; running the compressor at this frequency for a longer time would wear it out too much. The maximum frequency is thus given by

$$\tilde{f}(T_o, \dot{V}_a) = \begin{cases} f_2(T_o, \dot{V}_a) & \text{if } t < 30\,\text{min} \\ f_1(T_o, \dot{V}_a) & \text{if } t \geq 30\,\text{min} \end{cases}$$

The minimum frequency depends on the outdoor temperature, as in heating mode (fig. 3.3b).

(a) Heating mode

(b) Cooling mode
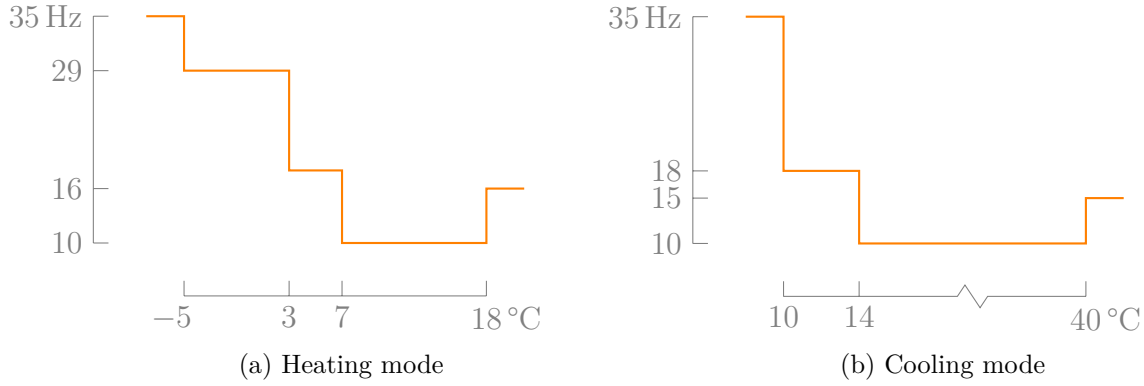
Figure 3.3: The compressor's minimum frequency f_0 is a function of the outdoor temperature.

The heat pump service instruction manual provides the function $f_2(T_o, \dot{V}_a)$ as a table. Surprisingly, there is no information about $f_1(T_o, \dot{V}_a)$, only a single value of $57\,\text{Hz}$. This value is however not supported by experimental results, as it can go up to $64\,\text{Hz}$ (see fig. 3.4). The frequency f_1 is thus computed as a scaled version of f_2: $f_1 = \frac{64\,\text{Hz}}{76\,\text{Hz}} f_2 = \frac{16}{19} f_2$.

The manufacturer's table describing $f_2(T_o, \dot{V}_a)$ is given in terms of the indoor unit fan setting
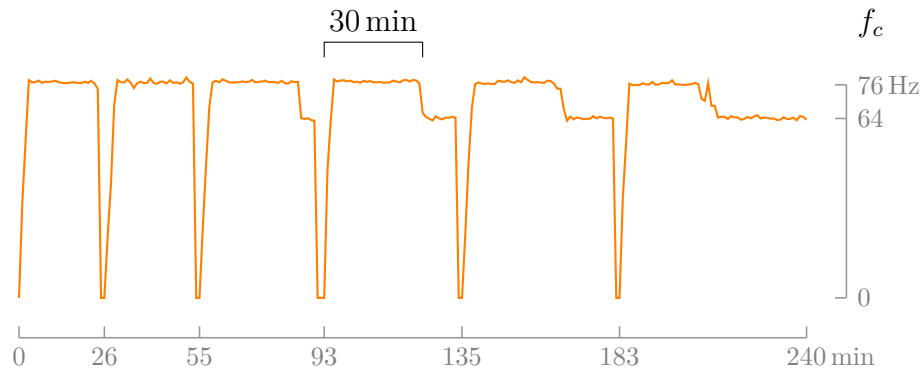
Figure 3.4: The compressor operates at a frequency $f_2 = 76\,\text{Hz}$ for 30 minutes—or until shutdown—then drops to a smaller value f_1 (in this case, $64\,\text{Hz}$).

(*high*, *medium*, *low* or *quiet*) and of outdoor temperature *zones*. The zone—and thus the frequency limit—is selected depending on the outdoor temperature value and on whether the temperature is increasing or decreasing, i.e. with a hysteresis property, as shown in fig. 3.5. For example, temperatures above 21 °C are all associated with zone A. When the temperature drops below 19 °C, the selected zone goes from A to B. To go back to zone A, the temperature has to rise above 21 °C. The boost frequencies observed during tests are in good accordance with the values provided by the manufacturer, at least for zones A and B. (There are very few tests with outdoor temperatures in zone C, since those temperature values are too low for typical cooling mode conditions.)

	High	Med	Low	Quiet
A	76	45	37	29
B	43	35	26	20
C	51	37	31	22
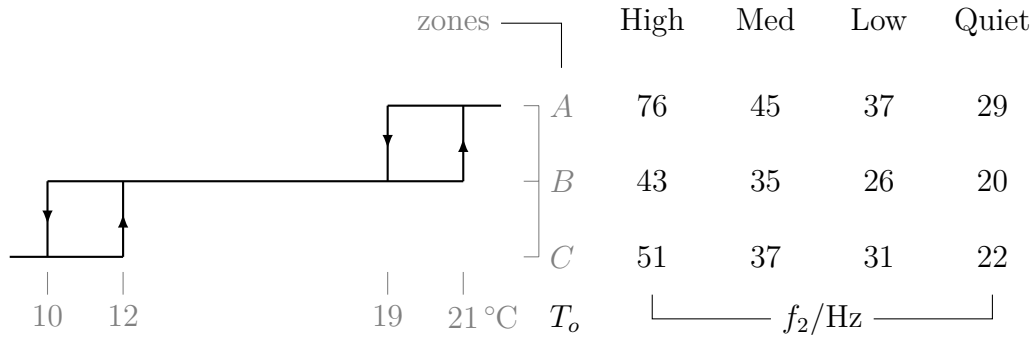
Figure 3.5: The boost frequency f_2 depends on the outdoor temperature and the indoor unit fan speed mode—figure adapted from [8].

3.1.3 Experimental observations

As a first observation, experimental results have shown that the heat pump frequency takes discrete values (fig. 3.6), although the service instruction manual does not provide any information about this. From a conceptual point of view, the compressor frequency can be seen as a quantized version of the saturated frequency (fig. 3.7).
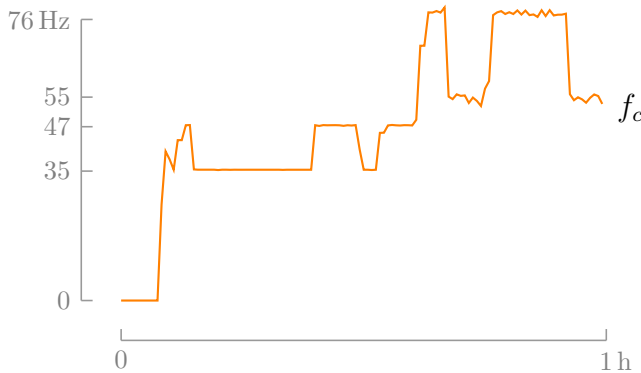
Figure 3.6: The compressor operates at predefined discrete frequency levels.
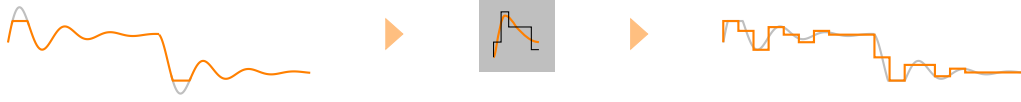
Figure 3.7: The compressor frequency is a quantized version of the saturated frequency signal.

The frequency is adjusted to get the command error e as low as possible and quickly respond to changes in environmental conditions to bring the heat pump in steady-state operation. There are however numerous cases where the heat pump does not behave as expected.

The most frequent type of unexpected behaviour is cycling. Even though the frequency is supposed to be varying continuously, the compressor is often in a situation where it shuts off for a few minutes then turns back on. There are two main causes to this cycling phenomenon, both of which are observed in fig. 3.8 for cooling operation. In this mode, according to the service manual, the heat pump should adjust its frequency when $e_{\min} \leq e \leq e_{\max}$ and shut down whenever $e > e_{\max} = 2\,°\mathrm{C}$. However, it seems that there is no upper deadband, i.e., $e_{\max} = 0\,°\mathrm{C}$, because the frequency falls to $0\,\mathrm{Hz}$ as soon as the error reaches $0\,°\mathrm{C}$. Even when $e_{\min} \leq e < 0\,°\mathrm{C}$, the frequency is kept at its maximum value, so unless the load is high enough, the heat pump switches off because the return temperature becomes too high. Indeed, the compressor frequency in fig. 3.8 is constant over a period of about five hours
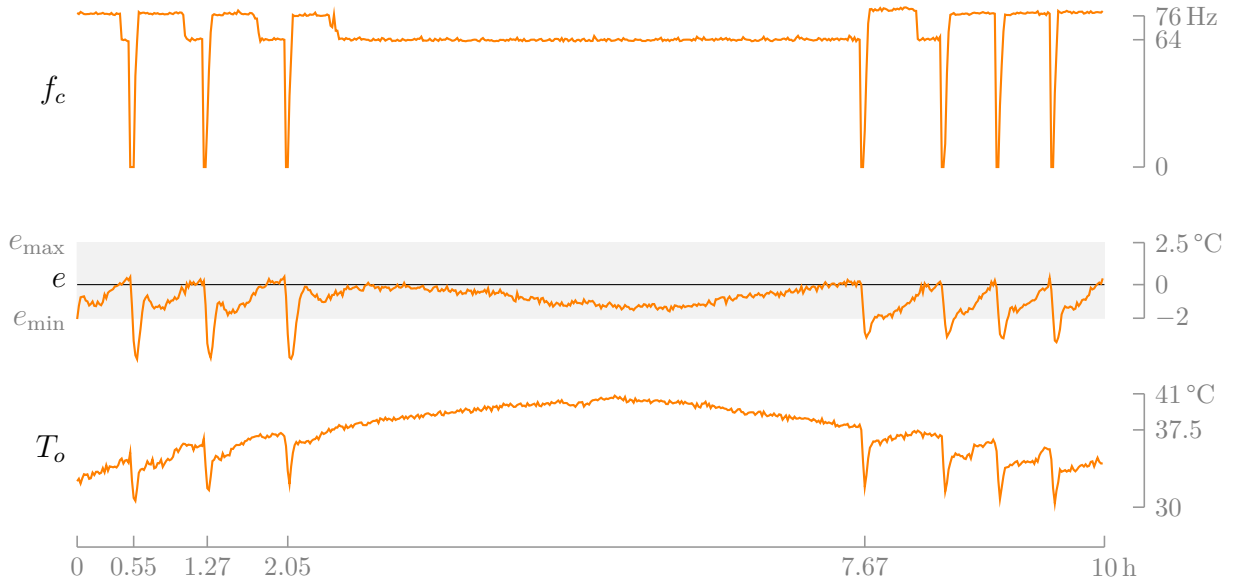
Figure 3.8: The heat pump switches off as soon as the error reaches $0\,°\mathrm{C}$, instead of $e_{\max} = 2.5\,°\mathrm{C}$ as it should according to [8]. Moreover, the compressor keeps operating at its maximum frequency, even after the $30\,\mathrm{min}$ boost and after the error falls in the range $e_{\min} \leq e \leq e_{\max}$. This causes cycling if the load in not high enough.

around the hottest time of the day. A high outdoor temperature increases the load and decreases the capacity of the heat pump, which is why the error is kept below $0\,°C$ over this period. As soon as T_o drops under $37.5\,°C$ though, the heat pump again begins to cycle instead of lowering the frequency.

A particular behaviour not mentioned in the service manual occurs for load values such that $e < e_{\min}$ when $f_c = f_1$, but $e \in [e_{\min}, 0\,°C]$ when $f_c = f_2$. Since the compressor cannot keep operating at f_2 for too long, it oscillates between f_1 and f_2. Each time the error drops below $e_{\min}$, the frequency jumps from f_1 to f_2, and some minutes after the error goes back above $e_{\min}$, it goes back to f_1. At this frequency level, the error then drops once again below $e_{\min}$ after a short period (fig. 3.9).
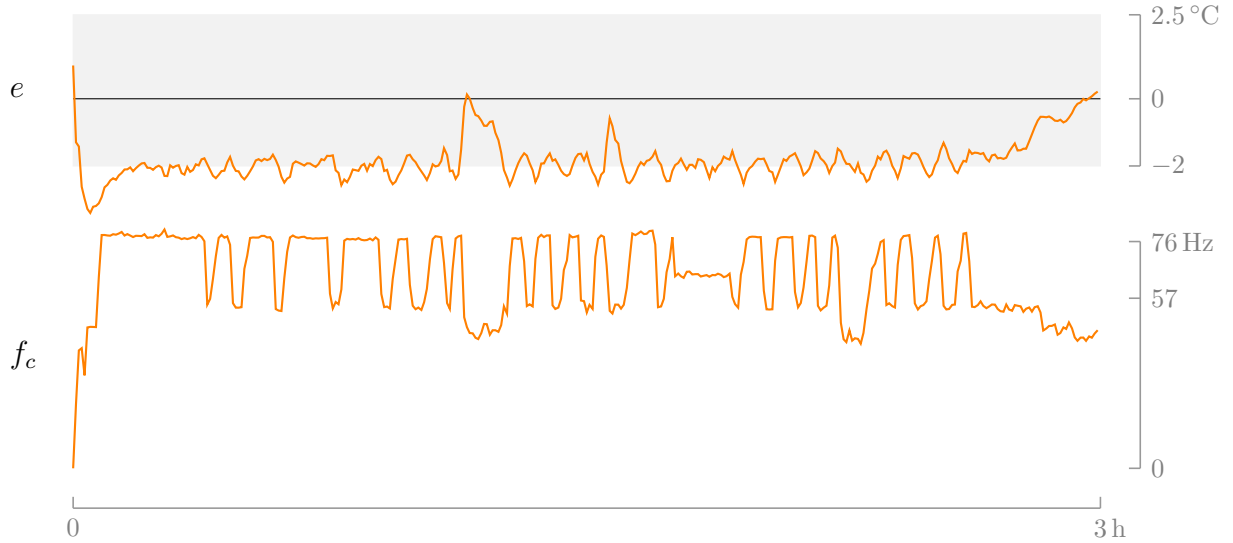
Figure 3.9: The compressor frequency oscillates when the load is just too high for the heat pump to keep the error above $e_{\min}$ when $f_c = f_1$.

If the load becomes low enough, the heat pump will still cycle but at a lower frequency (fig. 3.10). Moreover, the duration of the cycles is also not always the same. There are long cycles, whose duration are between 20 and $40\,min$, and short cycles, that last only a few minutes (about five in fig. 3.10). Fast cycling is found to occur more when the indoor fan unit mode is set to *high*, since the capacity increases with the air flow rate. The compressor frequency can take any (discrete) value during fast cycling, but during slow cycling, it always cycles at $f_c = \tilde{f}(T_o, \dot{V}_a)$.

At startup, the compressor is supposed to increase its frequency step by step over a period of $410\,s$. This behaviour is observed in heating mode (fig. 3.11) but not in cooling mode.
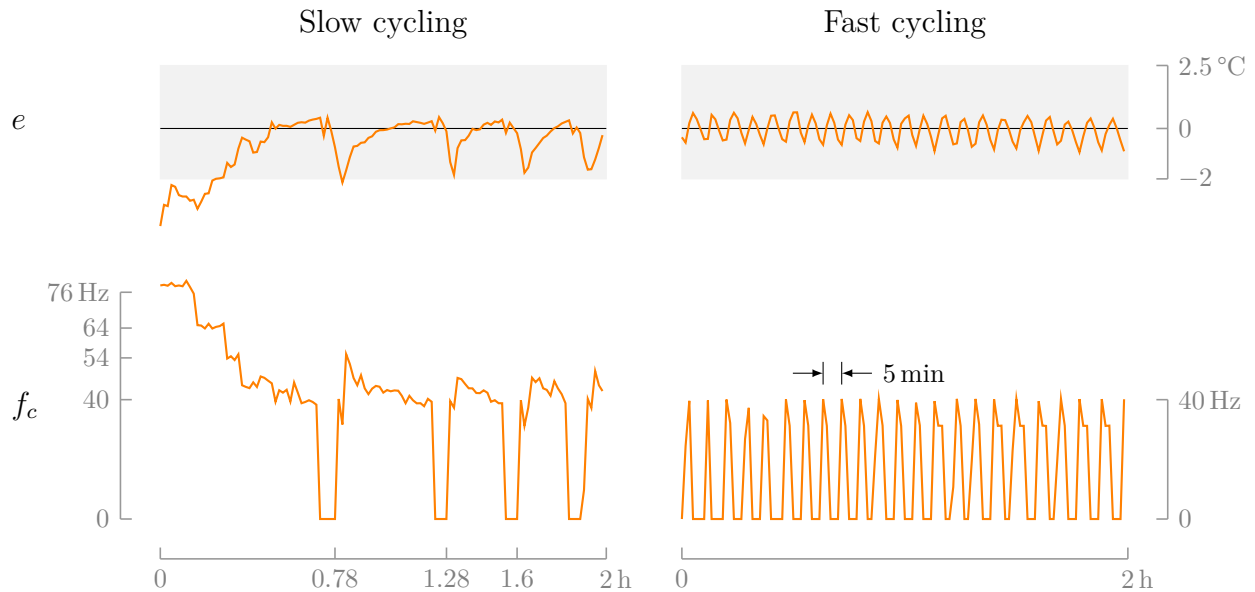
Figure 3.10: The compressor cycles at a lower frequency—about 40 Hz in this case—at lower loads. The cycling frequency can also vary, depending on the load and the indoor unit air flow rate. Note that, when fast cycling, the compressor does not "wait" for the error to drop below $e_{\min}$.
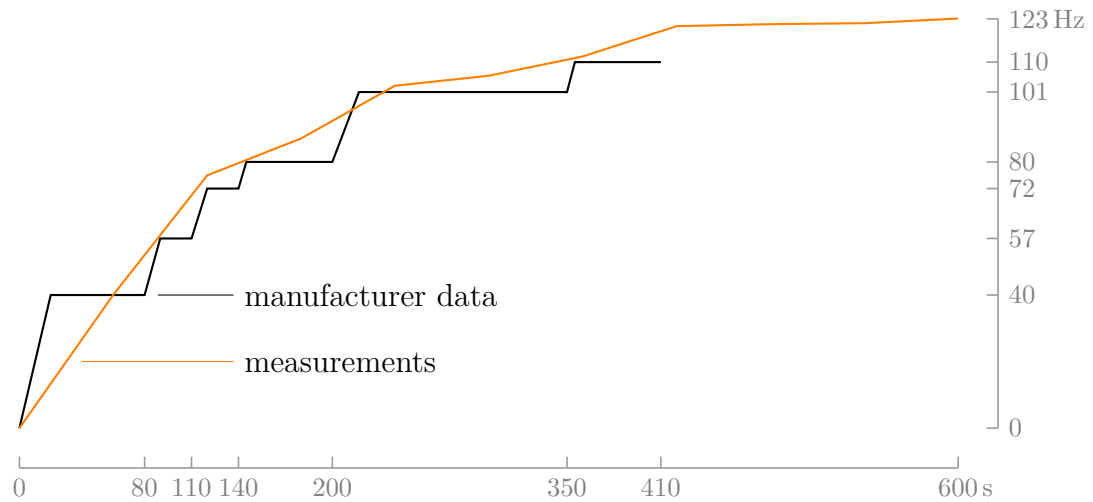
Figure 3.11: At startup, the compressor frequency increases gradually from 0 Hz to 110 Hz over a period of 410 s before reaching a steady-state.

3.2 Operating mode control

When it is not imposed by the user, the heat pump can choose the operating mode based on the error signal. The first criterion to select the operating mode is the error sign. If $e < 0\,°\mathrm{C}$, then T_r is too high and the heat pump should operate in cooling mode. If $e > 0\,°\mathrm{C}$, then T_r is too low and the heat pump should operate in heating mode. While this control strategy is fine when $|e| \gg 0\,°\mathrm{C}$, it can cause problems when T_r gets closer to the setpoint, that is, in normal room conditions. Since the operating mode is changed as soon as T_r crosses the setpoint, the controller switches modes very frequently as the error oscillates between negative and positive values. To avoid this undesired behaviour, the thermostat features a hysteresis on the error signal, with a width 2δ centered around $0\,°\mathrm{C}$ (see fig. 3.12). The tested heat pump's manual specifies a hysteresis half-width $\delta = 2\,°\mathrm{C}$. It also mentions that, unless the user imposes an operating mode, the thermostat waits for 6 minutes before checking again if the mode needs to be changed. This fixed mode minimum time is given as a parameter to the model.
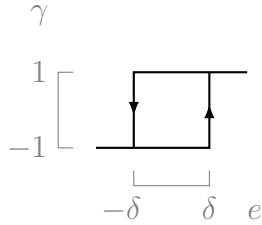
Figure 3.12: The thermostat uses hysteresis to avoid oscillations of the operating mode γ.

3.3 Fan speed mode control

Besides providing the air flow rate value to the heat pump component, the controller also needs the air flow rate to determine the boost frequency. As for the operating mode selection, the air flow rate is determined using hysteresis on the error signal. Since there are more than two speed levels, a cascading hysteresis is used, like for the zone temperature selection to calculate the boost frequency in fig. 3.5. The tested heat pump's error levels are given in fig. 3.13.

As fan speed modes labelled *low*, *medium* or *high* may correspond to different air flow rates for different heat pumps, it is preferable to use actual air flow rate values. These are usually provided by the manufacturer, although experimental values, if available, are preferred—they are not so easy to measure, and manufacturer values are not usually really accurate, as shown in table 3.1.

(a) Heating mode   (b) Cooling mode
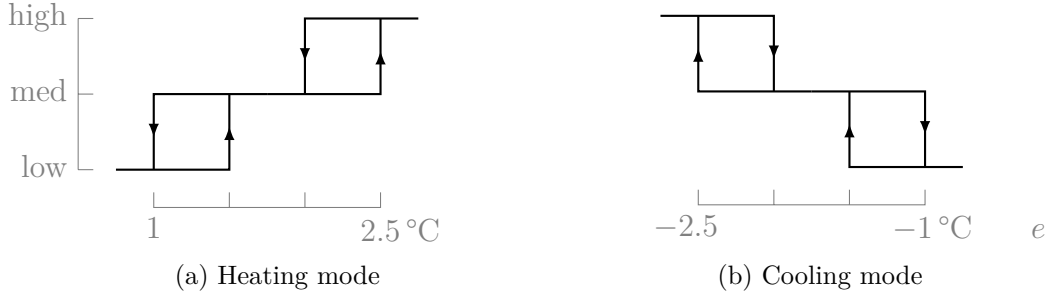
Figure 3.13: The manufacturer specifies as fan speed selection with two hysteresis loops in cascade.

Table 3.1: The relative difference between the air flow rate values provided by the manufacturer and the measurements is quite high.

Fan mode	Manufacturer values	Measurements	Relative difference	
High	$830 \, \mathrm{m^3 \, h^{-1}}$	$637 \, \mathrm{m^3 \, h^{-1}}$		$30\,\%$
Medium	$680 \, \mathrm{m^3 \, h^{-1}}$	$527 \, \mathrm{m^3 \, h^{-1}}$		$29\,\%$
Low	$580 \, \mathrm{m^3 \, h^{-1}}$	$442 \, \mathrm{m^3 \, h^{-1}}$		$31\,\%$
Quiet	$380 \, \mathrm{m^3 \, h^{-1}}$	$263 \, \mathrm{m^3 \, h^{-1}}$		$44\,\%$

3.4 Defrost mode control

The defrost operation and its impact on performance have been studied by St-Onge [10] for the same type of heat pump. The same modelling approach is used in this model, although with a slightly different implementation. The control component selects the defrost mode based on the outdoor temperature then passes it to the heat pump component which corrects the capacity and input power accordingly. The logic behind the mode selection has been reordered in a slightly different, more linear way, but it is strictly identical regarding the outputs.

A defrost cycle is divided in three parts. During the actual defrost operation, the heat pump works in cooling mode during a certain time τ_{df}. After switching back to heating mode, since the refrigerant was flowing in the opposite direction it undergoes transient phenomena decreasing the capacity for a period τ_{rec}. The capacity reduction is modelled by a *recovery penalty* $\epsilon \leq 1$ increasing with time. With t the time since the end of the last defrost and $\hat{t} \triangleq t/\tau_{\mathrm{rec}}$, the expression $\epsilon = 2\hat{t} - \hat{t}^2$ is used to compute the recovery penalty, so that $\epsilon(0) = 0$, $\epsilon(1) = 1$ and $\dot{\epsilon}(1) = 0$. Finally, there is a subsequent steady-state period τ_{ss}, and the duration

of a whole defrost cycle is $\tau_{\mathrm{df}} + \tau_{\mathrm{rec}} + \tau_{\mathrm{ss}}$.

The defrost pattern of the tested heat pump does not exactly follow the one observed by St-Onge, but it has defrost, recovery and steady-state periods as well (fig. 3.14).
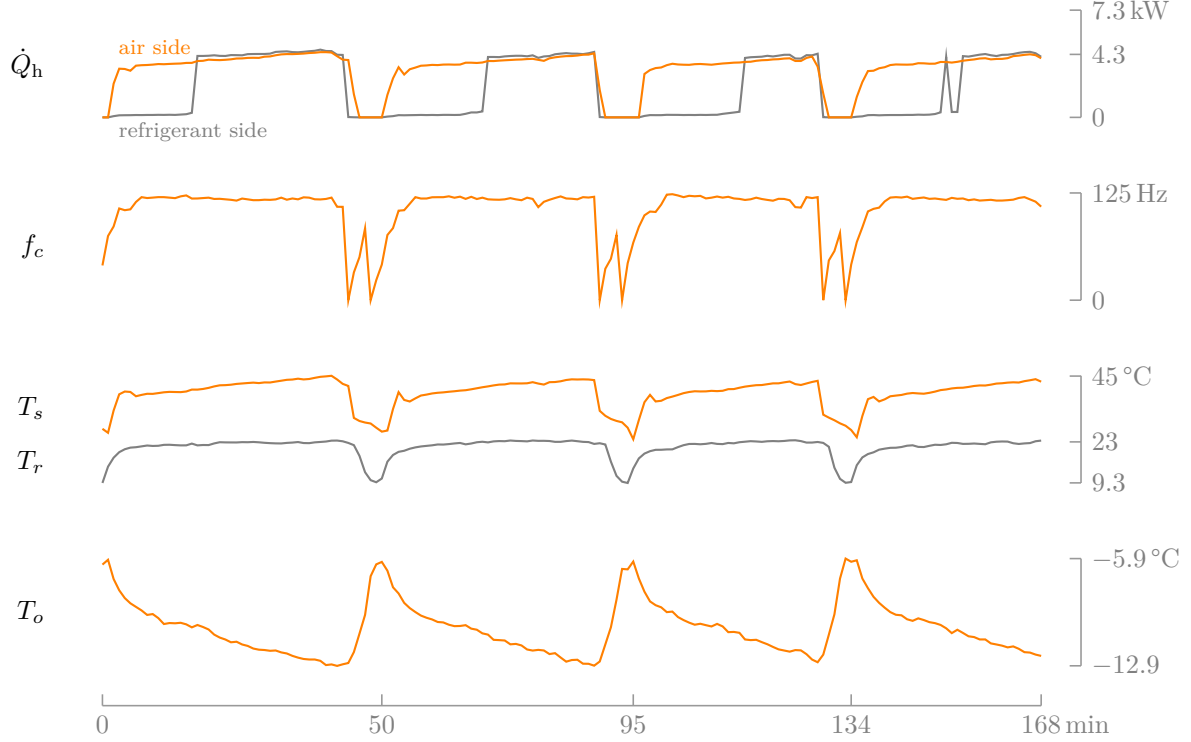
Figure 3.14: Defrost cycles can be divided in three parts: a frequency drop causing the return temperature to decrease significantly, a transient period where the capacity measured on the refrigerant side is much lower than that measured on the air side and a steady state period where both capacity measurements are approximately equals.

Because the duration of the different defrost cycle parts can vary, they are modelled a functions of the outdoor temperature—except for τ_{df} which has no apparent correlation with temperature, and is therefore assumed constant, at its average value of 4.64 min. The duration τ_{rec} appears to vary linearly within the range $-19\,°\mathrm{C} \leq T_o \leq 7\,°\mathrm{C}$ (fig. 3.15). It is given by

$$\frac{\tau_{\mathrm{rec}}}{\min} = \begin{cases} 10.798 - 0.9315\,\dfrac{T_o}{°\mathrm{C}} & \text{if } T_o \geq -28\,°\mathrm{C} \\ 37 & \text{if } T_o < -28\,°\mathrm{C} \end{cases}$$

To determine the steady-state duration, the heating time of a defrost cycle $\tau_{\mathrm{h}} = \tau_{\mathrm{rec}} + \tau_{\mathrm{ss}}$ is determined as a function of the outdoor temperature. Unlike the recovery time, measurements are quite noisy, but a curve is outlined by dropping some outliers (fig. 3.16).

The regression is given by

$$\frac{\tau_\mathrm{h}}{\min} = 37.387 + 16.638 \, \exp\left[0.235\left(\frac{T_o}{°\mathrm{C}} - 2.118\right)\right]$$
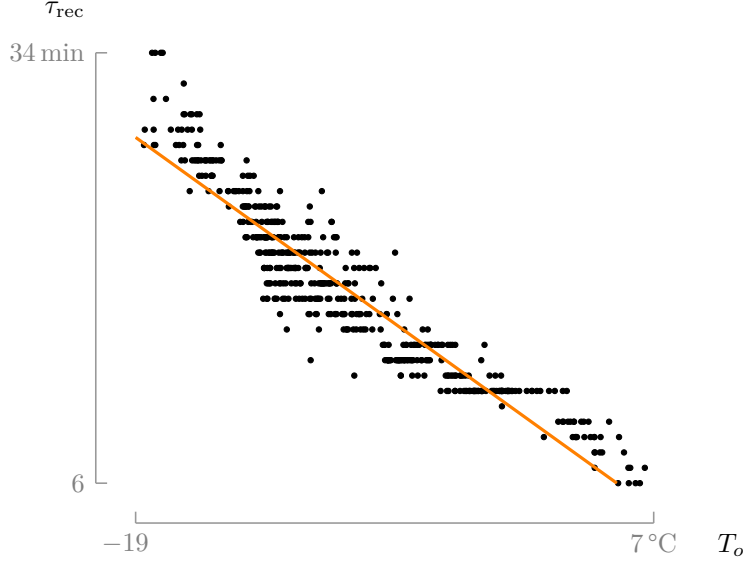
Figure 3.15: The recovery time has a strong linear correlation with the outdoor temperature. The apparent discrete levels result from the sampling rate $1\,\mathrm{min}^{-1}$.
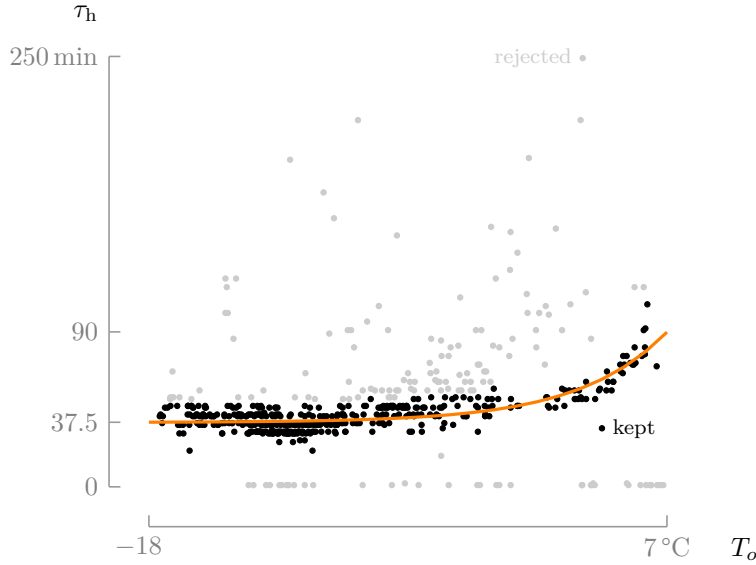
Figure 3.16: At cold temperatures, τ_h is lower so the defrost cycle frequency is higher. However, the water content of the air is lower so there is little variability. At higher temperatures, the heating time increases with T_o following an exponential trend.

To sum up, a defrost cycle is modelled using three different defrost modes:

1. During defrost operation, there is no output heat ($\dot{Q}_\mathrm{h} = 0$) and a correction factor of $60\,\%$ is applied to the power draw, as mentioned in [10, section 4.4].

2. When operating in recovery mode, the heat pump draws the same amount of power than in steady-state, but the capacity is affected by a factor ϵ.

3. In steady-state, both the power and capacity values are those normally interpolated from the heating performance map.

The durations τ_{df}, τ_{rec} and $\tau_{\mathrm{ss}} = \tau_{\mathrm{h}} - \tau_{\mathrm{rec}}$ associated with each defrost mode may vary with the outdoor temperature.

3.5 Summary

In conclusion, some control rules defined in the service instruction manual agree well with the measurements (boost frequency, lower error limit, startup ramp), but not all of them. In particular, the upper error limit e_{max} is often zero, which seems to be the main cause of unexpected cycling. This cycling is observed more frequently when the fan speed is set to *high*, likely because at this speed the boost frequency—and thus also the capacity—is higher (fig. 3.5), causing the error limits to be reached faster. The cycling observed on the tested heat pump is different from that of a fixed capacity heat pump, because the capacity level at which cycles occur can vary. This cycling causes a performance degradation compared to a situation where the capacity is varying smoothly, but it has a lower frequency compared to a fixed capacity heat pump. Finally, regressions are obtained from experimental results to compute the defrost parameters.

CHAPTER 4   PERFORMANCE

As the model relies on measured performance data, this data should be as complete and accurate as possible. Manufacturer data, which have the advantage of being already available, unfortunately lack accuracy, and especially completeness [2,10]. This stems from the multiple environment variables that need to be considered, resulting in a high number of combinations (see fig. 4.1). To establish a more adequate performance map, experimental tests have been conducted on two different VCAAHPs at the CanmetENERGY research centre in Varennes, QC. The first heat pump has been analyzed by St-Onge [10] and was used for the first version of the VCAAHP model. The second heat pump testing is detailed in this chapter.
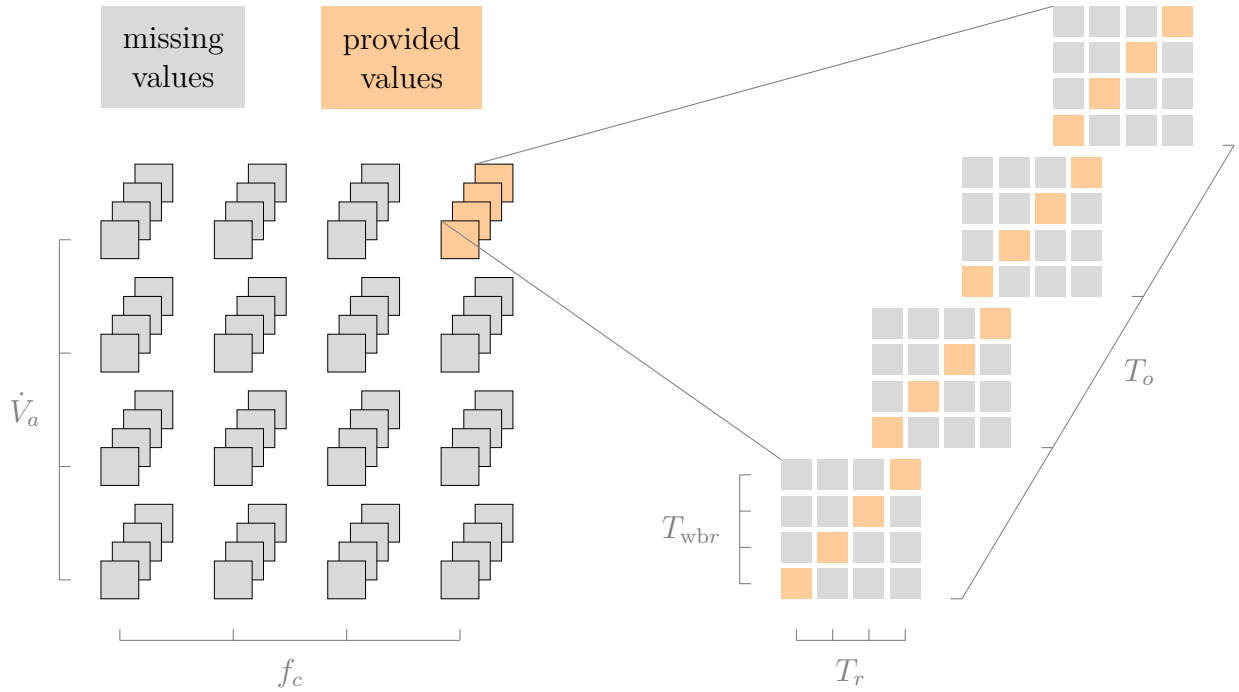
Figure 4.1: A large amount of data is usually missing from manufacturer manuals. For the tested heat pump, only two out of the five dimensions required for the performance map are covered. For each pair $(f_c, \dot{V}_a)$, a matrix should provide performance as a function of T_r and $T_{\mathrm{wb}r}$ for each value of T_o. In the case of table B.1, only one air flow rate value is provided, but no frequency values are given—so rated frequency is assumed. For each matrix $(T_r, T_{\mathrm{wb}r})$, only diagonal values are provided.

Of course, most users of the model will not have access to experimental data, which makes the model useless if they cannot provide a complete performance map. Regressions are thus deduced from experimental results to extrapolate data that is usually missing.

In addition to supplementing manufacturer data, experimental tests also help understand how the heat pump operates and confirm whether the control rules are followed in practice. However, all the different control mechanisms often get in the way of the primary objective (measuring performance) and setting the right testing conditions is sometimes challenging, especially since many of those mechanisms remain unknown. It should be noted that the heat pump is designed for field usage and cannot be easily tested in a laboratory. However, this fact implies that performance cannot be evaluated for each environmental conditions combination, i.e. for each square cell in fig. 4.1. This is apparent especially in global test results, e.g. when looking at the frequency distribution in fig. 4.2. Therefore, assumptions are made to develop the regressions with fewer data, then use those to generate a complete performance map for the tested heat pump.

Since there are different things to consider depending on the operating modes, heating and cooling operation are treated separately.

4.1 Heating operation

An overview of the heating test results is depicted in fig. 4.2. The operating ranges are more or less in accordance with manufacturer rated operation limits, $T_o \in [-26\,°\text{C}, 24\,°\text{C}]$ and $\dot{Q}_\text{h} \in [0.9\,\text{kW}, 6.48\,\text{kW}]$.
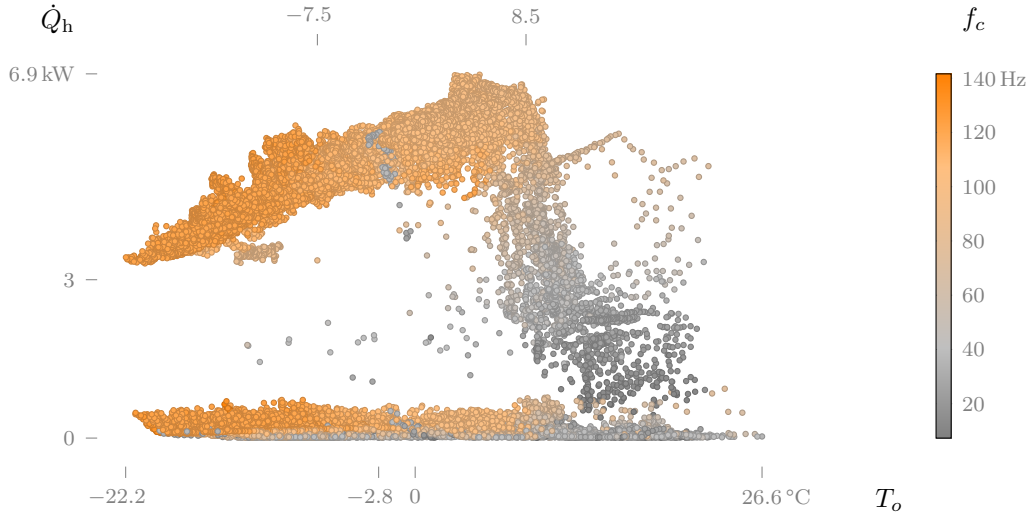
Figure 4.2: The heating capacity increases with the outdoor temperature at a rate of about $1\,\text{kW}/10\,°\text{C}$. Above $8.5\,°\text{C}$, the compressor frequency drops suddenly and thus also the capacity. There are also many low capacity values (between 0 and $500\,\text{W}$) at a high frequency which are independant of T_o. These stem from the transient regime occurring at startup illustrated in fig. 3.14.

Besides the transient regime data in the range $[0\,\mathrm{W}, 500\,\mathrm{W}]$, three groups can be isolated. First, in the range $T_o \in [-22.2\,°\mathrm{C}, -7.5\,°\mathrm{C}]$, high frequencies are observed along with a slope $\frac{d\dot{Q}_\mathrm{h}}{dT_o}$ that is quite steep. Second, in the range $T_o \in [-7.5\,°\mathrm{C}, 8.5\,°\mathrm{C}]$, the frequencies are slightly lower—though still high—and the slope a little less steep. Finally, in the range $T_o \in [8.5\,°\mathrm{C}, 26.6\,°\mathrm{C}]$, the frequency and capacity completely drop: the slope is negative and much steeper than for the two other groups.

The slope in the second group is lower than in the first one, because in this temperature range, the heat pump can still respond to a temperature drop by increasing the compressor frequency and thus the capacity. In the first group however, the capacity is maxed out so it decreases with the temperature as a fixed-capacity heat pump would. The drop in the third group can be explained by the fact that the need for heating decreases as the outdoor temperature gets closer to the setpoint—although it is not clear why the curvature is so important.

Data restricted to steady-state values[1] and the same indoor temperature range as in the manufacturer data is presented in fig. 4.3. Figure 4.2 shows a clear distribution of performance points according to the frequency. On the other hand, fig. 4.3 does not show a clear impact of T_r on the performance.
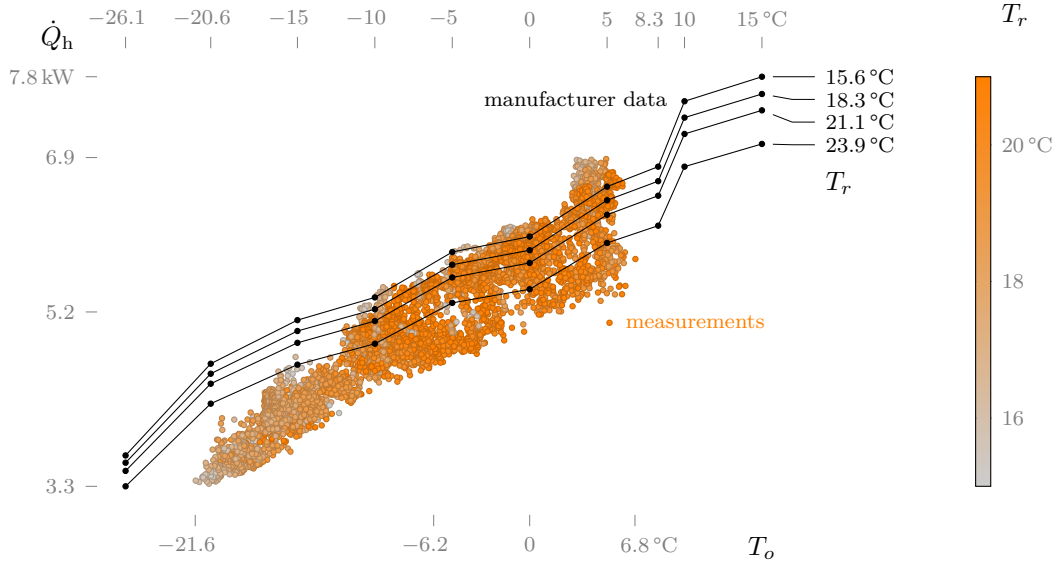
Figure 4.3: The manufacturer values are in good accordance with the steady-state capacity measurements at mild outdoor temperatures but seem somewhat overestimated in colder conditions.

[1]Results show that the frequency is a good indicator of the overall regime of the heat pump; they are thus considered in *steady-state* when the frequency variance is limited to $2\,\mathrm{Hz}$ for at least $30\,\mathrm{minutes}$.

The measured COP seems more in line with the manufacturer values than the capacity at cold temperatures (fig. 4.4). Even though the compressor is usually running at maximum frequency in this temperature range, this means that the input power decreases even more than the capacity. A possible cause for this efficiency gain is mentioned in [11, section 11.4]. When the compressor loses heat to its environment, the refrigerant entropy at the compressor outlet is lower than it would have been in adiabatic conditions. At cold temperatures, the entropy loss becomes significant compared to the entropy gain from frictional effects, thus $s_2 < s_1$ (whereas $s_2 > s_1$ at mild outdoor temperatures). Reducing the entropy means that the specific volume of the refrigerant v decreases, and the input work as well since $w = \int_1^2 v\,dp$. In conclusion, at cold temperatures manufacturer data overestimate the power input because of the efficiency gain, but heating capacity is also overestimated which results in matching COP values.
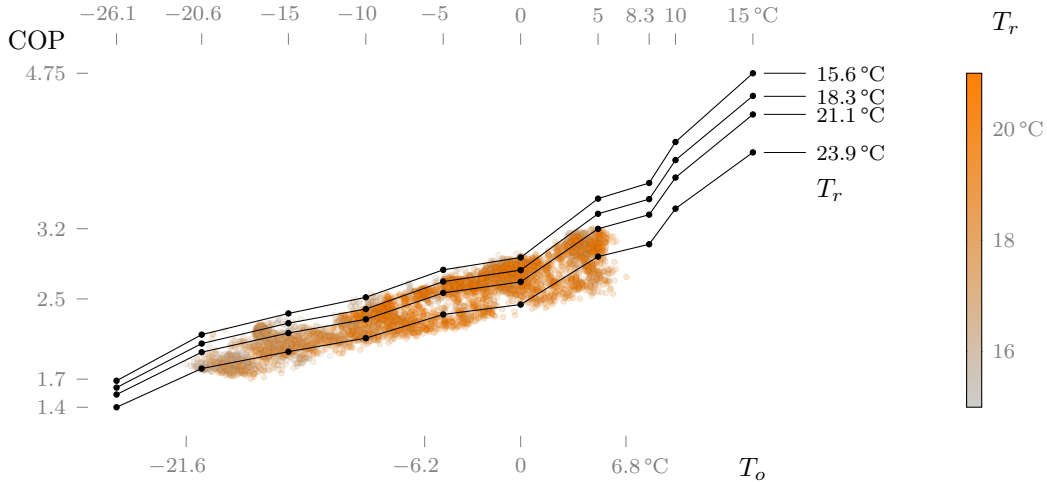
Figure 4.4: At cold outdoor temperatures, the COP measurements are closer to manufacturer values than steady-state capacity measurements (fig. 4.3), because the power input is overestimated as well.

The main missing information in manufacturer data is the frequency dependency. As mentioned above, the frequency values depend strongly on T_o and T_r, and the relation $\dot{Q}_{\mathrm{h}}(f_c)$ thus cannot be obtained for each environmental condition. A different approach is therefore followed: the frequency is separated from the other performance map variables, so that

$$\dot{Q}_{\mathrm{h}}(T_r, T_o, \dot{V}_a, f_c) = \dot{Q}(T_r, T_o, \dot{V}_a)\ \varphi_{\mathrm{h}1}\left(\frac{f_c}{\tilde{f}}\right)$$

and finding the frequency dependency then comes down to establish the function $\varphi_{\mathrm{h}1}$ only for one set of variables $(T_r, T_o, \dot{V}_a)$. The main simplifying assumption is that the function $\varphi_{\mathrm{h}1}$ has

the same shape for any operating conditions $(T_r, T_o, \dot{V}_a)$. This assumption is, for example, present in the manufacturer data for the heat pump tested by St-Onge [10], as discussed below (see fig. 4.11). Note that the frequency is normalized by the maximum frequency value $\tilde{f} = 119\,\mathrm{Hz}$ since it is the only one provided in the service instruction manual, and supposedly the one for which the performance data is provided. In what follows, the shorter notation $\nu \triangleq f_c/\tilde{f}$ is used. Outdoor humidity has an impact on performance through defrost cycles and thus needs to be considered when simulating *transient* processes. It has however no significant influence on steady-state performance, so it is not included in the performance map variables; it makes more sense to let the controller component handle the humidity impact on performance.

Looking at the global heating data in fig. 4.2, the only dataset suitable to compute $\varphi_{\mathrm{h1}}(\nu)$ corresponds to the steep capacity drop at $T_o > 8.5\,°\mathrm{C}$. Indeed, it is the only one featuring a broad frequency range at (more or less) constant environmental conditions. By restricting the data to steady-state values and $T_o = 9\,°\mathrm{C} \pm 1\,°\mathrm{C}$, it appears that the capacity changes with the frequency in an almost—but not quite—linear trend (fig. 4.5). The lack of low frequency values (between 0 and 39.5 Hz) in these conditions is compensated by imposing that $\dot{Q}_{\mathrm{h}} = 0$ at $f_c = 0\,\mathrm{Hz}$. A second-order polynomial thus seems a reasonable choice for $\varphi_{\mathrm{h1}}(\nu)$. The polynomial coefficients can be obtained by minimizing the least-squares error, under the two constraints that

1. the value of $\dot{Q}_{\mathrm{h}}$ is zero at $f_c = 0$, i.e. $\varphi_{\mathrm{h1}}(0) = 0$; and

2. the capacity at $\nu = 1$ (not in the range of fig. 4.5) is that provided by the manufacturer, which is about 6.5 kW, so that $\dot{Q}_{\mathrm{h}} = \varphi_{\mathrm{h1}}(\nu) \cdot 6.5\,\mathrm{kW}$ and $\varphi_{\mathrm{h1}}(1) = 1$.
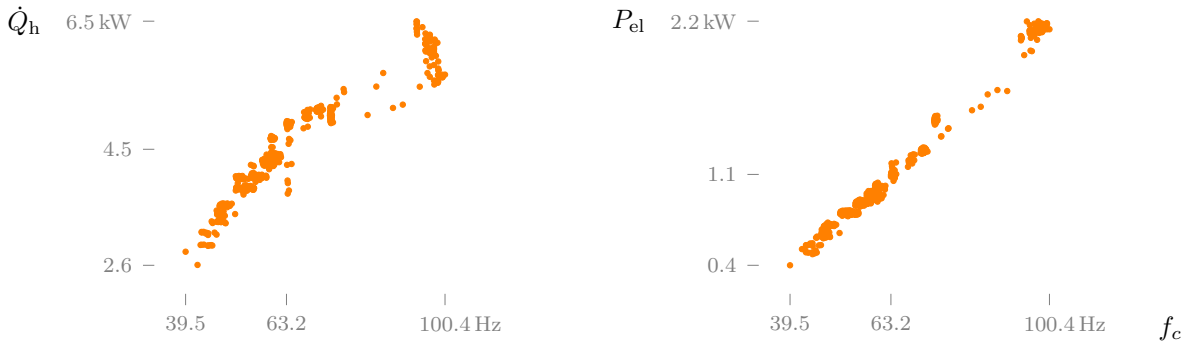
Figure 4.5: The heating capacity increases with the frequency with a curvature that is slightly negative. The total input power on the other hand shows no curvature since the compressor power draw is proportional to its speed [12].

The polynomial coefficients can easily be found using for example the method of Lagrange multipliers (fig. 4.6).

As opposed to the capacity, the total input power has no curvature. It cannot however be approximated by a straight line, since this would give negative power values at low frequencies. Instead, it includes a correction term to keep positive values:

$$\varphi_{h2}(\nu) = a\nu - b + ce^{-d\nu}$$

As for the capacity, the constraint $\varphi_{h2}(0) = 0$ is enforced, hence $c = b$. To ensure that $\varphi_{h2} \geq 0$, the following constraint is added

$$\left.\frac{d\varphi_{h2}}{d\nu}\right|_{\nu=0} = 0 \Rightarrow d = a/c$$

Thus,

$$\varphi_{h2}(\nu) = a\nu - b\left[1 - \exp\left(-\frac{a\nu}{b}\right)\right]$$

At higher frequencies, $\varphi_{h2} \approx a\nu - b$, and the parameters a and b are selected to best fit the data (fig. 4.6). After performing the regressions, the capacity and power corrections are found to be

$$\varphi_{h1}(\nu) = 1.676\nu - 0.676\nu^2$$

$$\varphi_{h2}(\nu) = 1.524\nu - 0.561\left[1 - \exp\left(-\frac{1.524\nu}{0.561}\right)\right]$$
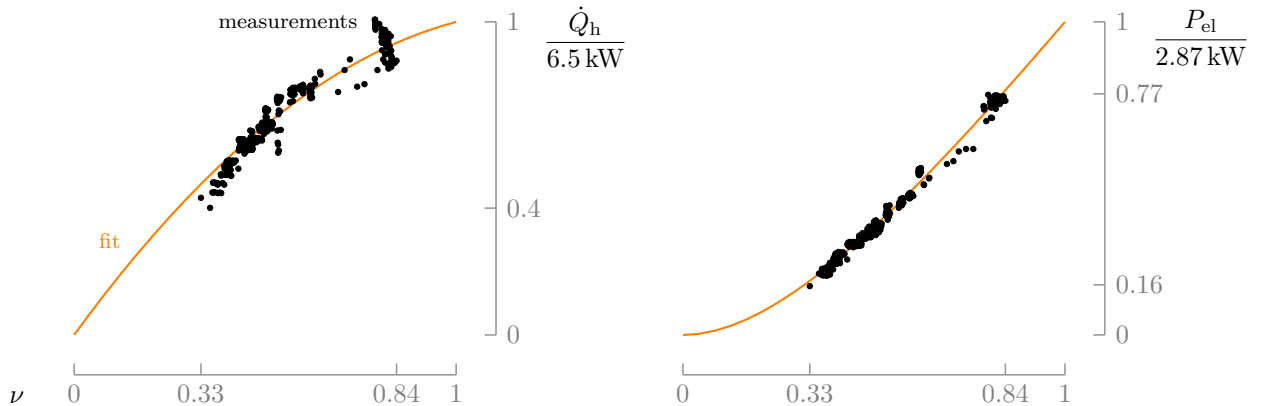
Figure 4.6: The functions φ_{h1} and φ_{h2} fit the measurements with a minimal least-squares error while respecting the constraints.

4.2 Cooling operation

The steady-state measured capacity values in cooling mode are more spread out than in heating mode. In particular a high concentration of points are located above the manufacturer values, because the compressor often operates at the boost frequency for a significant fraction of the test duration.
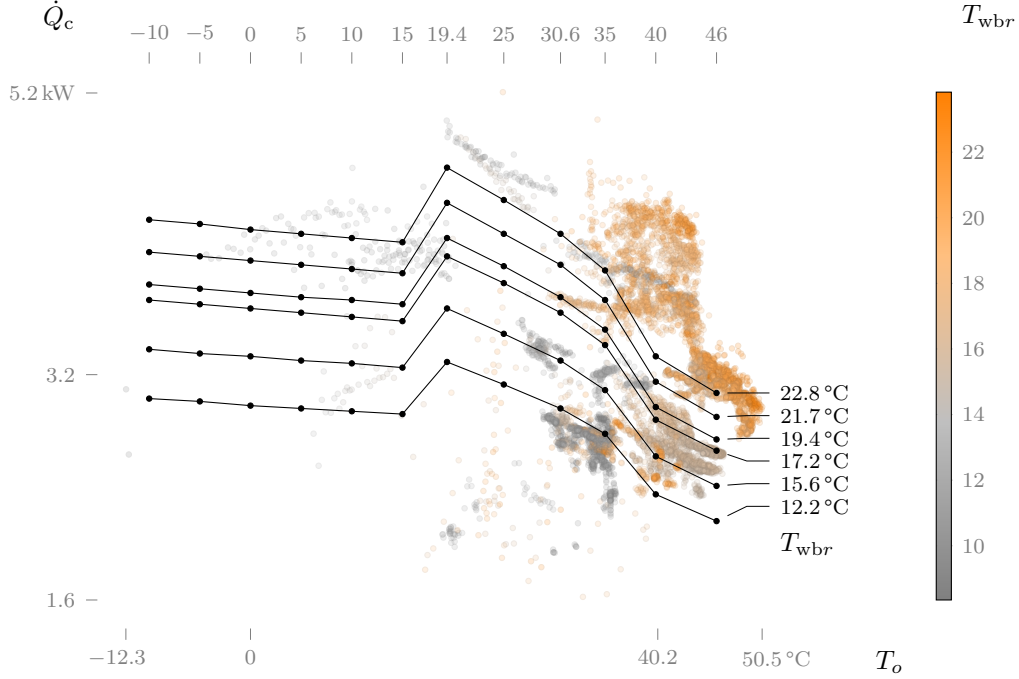
Figure 4.7: In the temperature range above 19.4 °C, the capacity is decreasing with increasing outdoor temperature. Below this temperature, there is almost no variation except between 15 and 19.4 °C, where the capacity rises suddenly. Capacity values below 19.4 °C are not really of concern, because it is unusual to operate in cooling mode at such temperatures, which is why there are very few data points.

The frequency dependency in cooling mode is expressed the same way as in heating mode, by separating variables. The frequency is normalized using the manufacturer provided steady-state maximum value, $\nu = f_c/f_1$ with $f_1 = 57\,\mathrm{Hz}$. At this frequency, the reference capacity found by using the fit is $3.6\,\mathrm{kW}$ (fig. 4.8).

The frequency correction is given by $\varphi_{c1}(\nu) = 1.059\nu - 0.059\nu^2$.

The correction on power consumption φ_{c2} has the same form as in heating mode, since the values also follow a linear trend, and there is not enough data at low frequencies. The
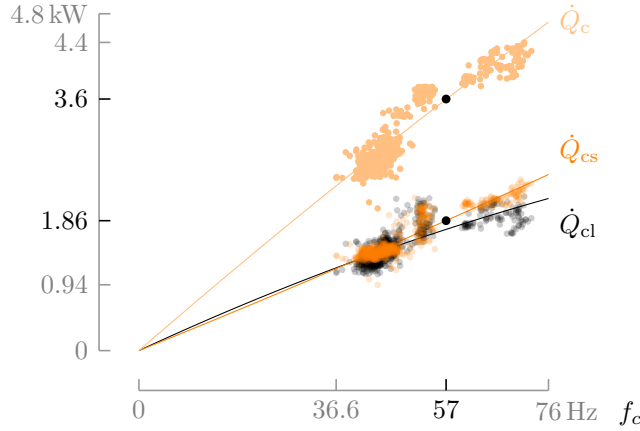
Figure 4.8: At $T_r = 23\,°C$, $T_{wbr} = 17\,°C$, $T_o = 40\,°C$ and $f_c = 57\,Hz$—the assumed operating frequency for which manufacturer data are provided—the total cooling capacity announced by the manufacturer ($2.88\,kW$) is $20\,\%$ lower than the measured value, while the sensible capacity ($2.5\,kW$) is $34\,\%$ higher. Manufacturer data thus seem to underestimate the capacity but also the latent part.

regression yields a nominal value of $0.96\,kW$ and the following correction (depicted in fig. 4.9):

$$\varphi_{c2}(\nu) = 1.363\nu - 0.372 \left[1 - \exp\left(-\frac{1.363\nu}{0.372}\right)\right]$$
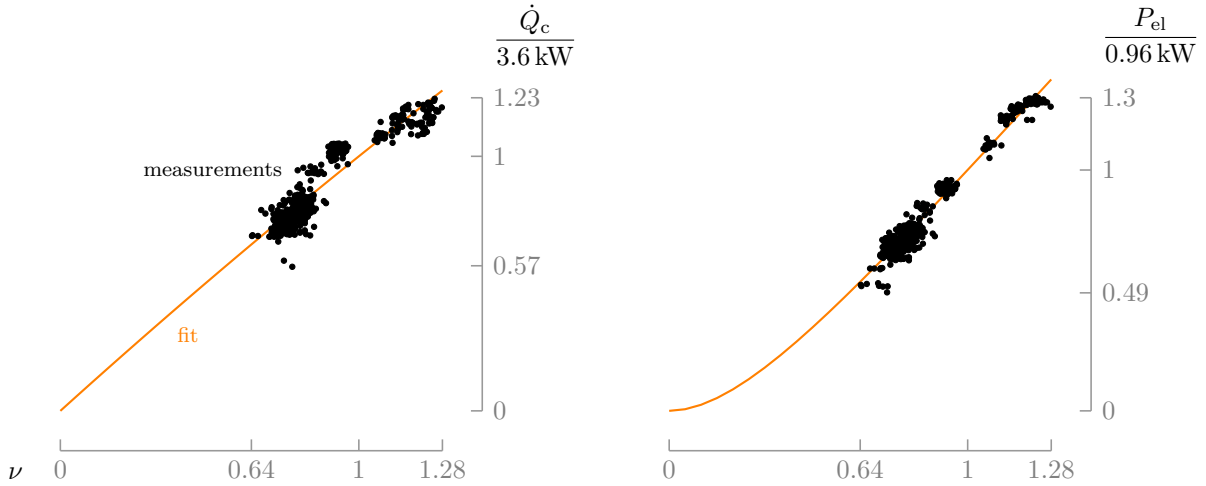
Figure 4.9: The capacity shows less curvature in cooling mode than in heating mode, hence the small square term in φ_{c1}. A large number of points are located above $\nu = 1$, which is representative of the heat pump tendency to often operate at its boost frequency level.

Another correction is provided in order to quantify the impact of humidity. The variable used to quantify the humidity is the wet-bulb depression, $\Delta T_r \triangleq T_r - T_{wbr}$. It has the advantages of being easy to compute using T_{wbr} which is a performance map entry, but unlike T_{wbr} it reflects the degree of saturation in the air. Close to the saturation (at low ΔT_r), the latent load is higher so the SHR—as defined in eq. (2.1)—is low. As ΔT_r increases, the humidity content decreases so the SHR increases, getting closer and closer to 1 (fig. 4.10). The SHR

fit is given by

$$\text{SHR} = 1 + 0.6 \left[\tanh \left(0.144 \frac{\Delta T_r}{°\text{C}} - 0.724 \right) - 1 \right] \tag{4.1}$$

and thus the capacities are

$$\dot{Q}_{\text{cs}} = \dot{Q}(T_r, T_o, \dot{V}_a) \, \varphi_{\text{c1}}(\nu) \, \text{SHR}(T_r, T_{\text{wb}r})$$
$$\dot{Q}_{\text{cl}} = \dot{Q}(T_r, T_o, \dot{V}_a) \, \varphi_{\text{c1}}(\nu) \, [1 - \text{SHR}(T_r, T_{\text{wb}r})]$$

Figure 4.10: To account for the humidity in evaluating performance, the SHR is obtained as a function of the wet-bulb depression ΔT_r.
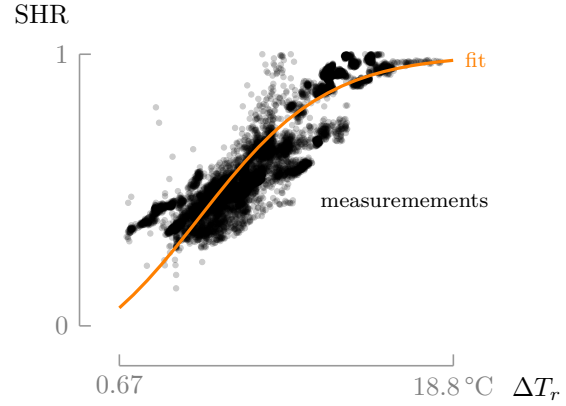
Manufacturers sometimes provide a frequency correction such as those of figs. 4.5 and 4.8. For example, fig. 4.11 shows manufacturer regressions resembling those that were found. Data for the SHR values can also be found, for example [13] provide example data (see appendix A) with a shape similar to what is observed in fig. 4.10.
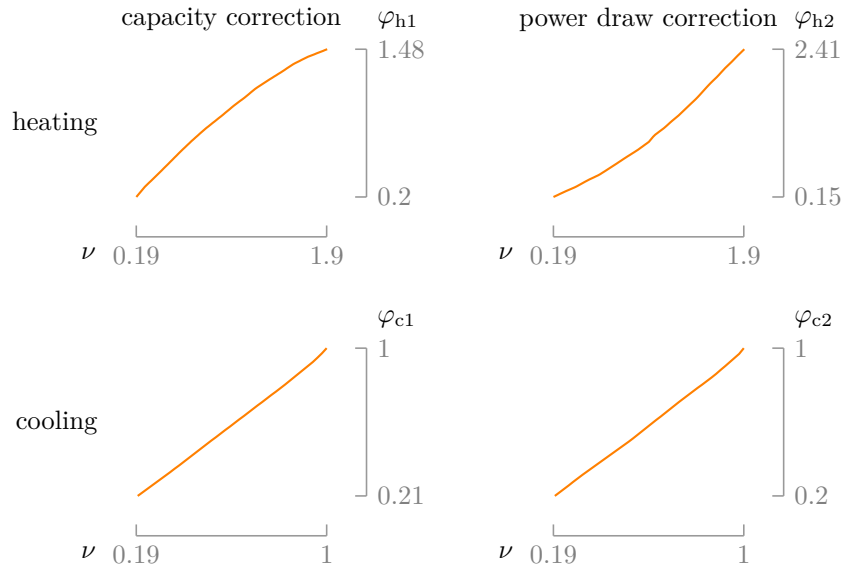
Figure 4.11: The capacity and power draw corrections by frequency from the Mitsubishi MUZ-FE12NA heat pump have a shape relatively similar to those obtained from experimental results—adapted from [14].

4.3   Summary

Experimental results were compared to manufacturer data and used to obtain regressions to extend the performance map. Manufacturer heating capacity values match the measurements quite well at mild outdoor temperatures, but they are slightly overestimated below $10\,°C$. The COP values on the other hand seem to agree well over the temperature range $-21.6\,°C \leq T_o \leq 6.8\,°C$. Cooling capacity data points are more dispersed, and many points corresponding to boost frequency mode are located above the manufacturer curves. Although they do not follow a trend as obvious as in heating mode, they seem to evolve in the same way as the manufacturer capacity values.

Regressions were found from experimental data to correct performance values at different frequencies and determine the sensible and latent fractions of the cooling capacity based on the indoor wet-bulb depression ΔT_r. With those regressions in hand, it is now possible to extend the performance map. Examples are shown in figs. 4.12 to 4.14. This determines, along with the control rules of chapter 3, the way that the model will behave.
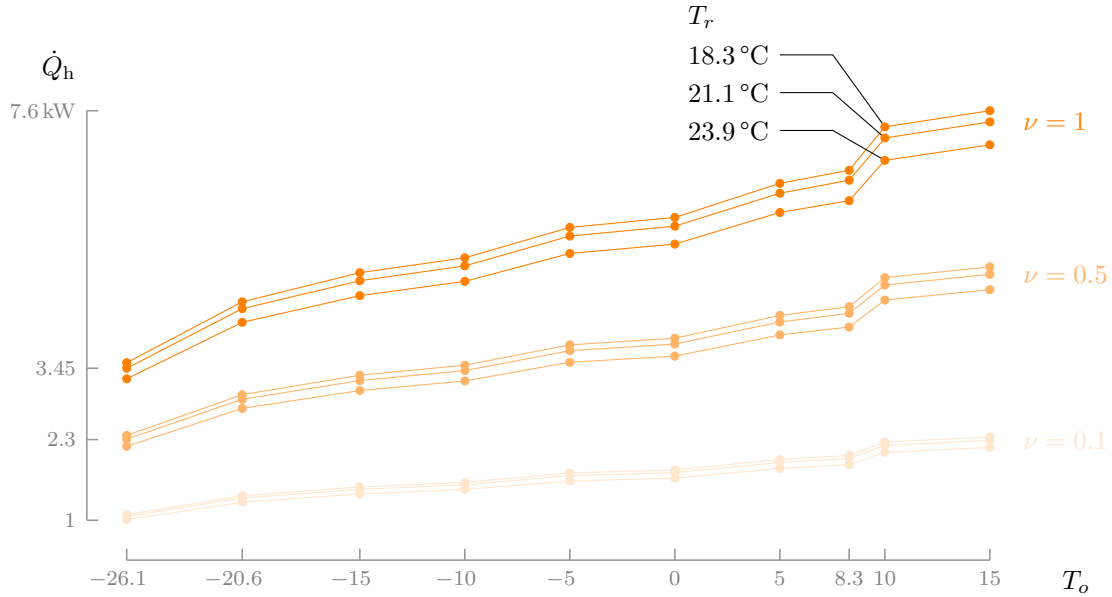
Figure 4.12: The extended performance map adds groups of lines at different frequencies to the manufacturer data in fig. 4.3.
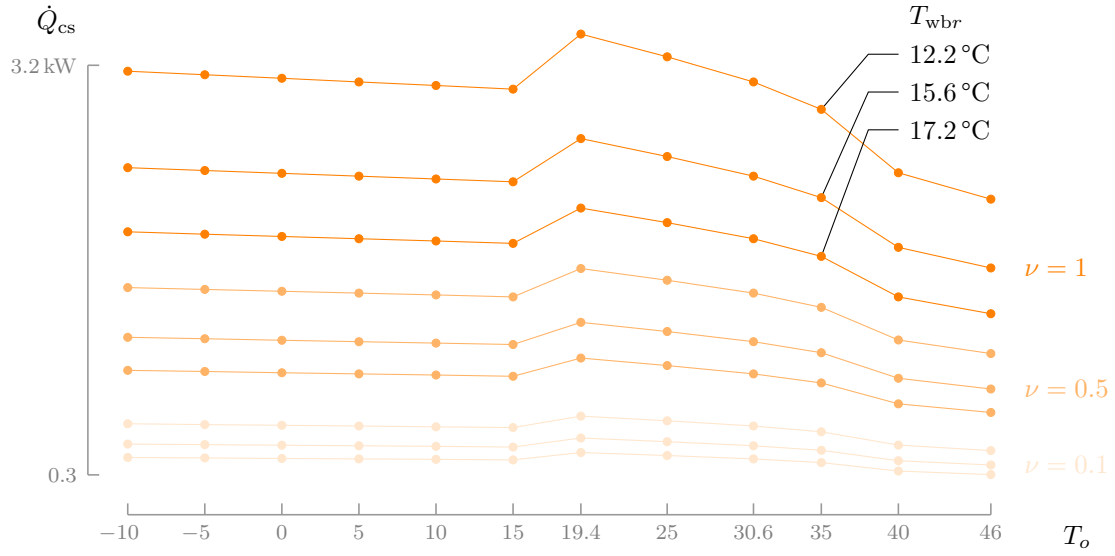
Figure 4.13: This "slice" of the performance map (at $T_r = 23.9\,°\mathrm{C}$) is obtained from φ_{c1} and the SHR.
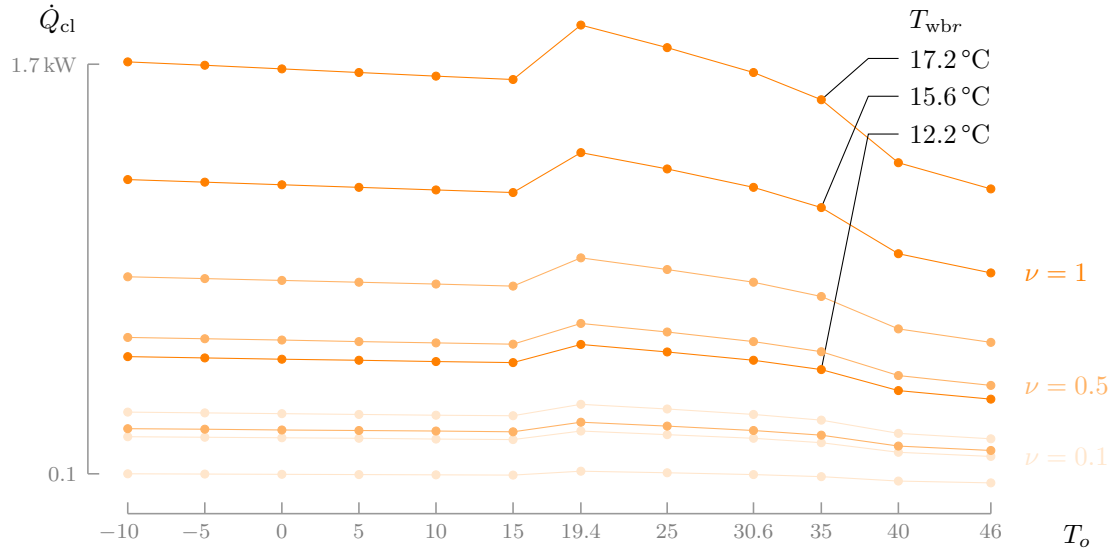
Figure 4.14: The latent capacity has a similar shape to the sensible capacity, since they are scaled by the SHR which does not depend on T_o.

CHAPTER 5   MODEL

The model operations can be divided into three main categories. First, the compressor frequency is computed according to control strategies, input values and a setpoint. Then, performance data is interpolated from the performance map and the input values. Finally, outlet air state and several additional outputs such as the COP are computed based on those interpolated values.

Control strategies may vary depending on the heat pump model. Accordingly, a user may want to define their own, corresponding to the heat pump model they wish to simulate. To allow utilization of custom control strategies, the control part is separated from the rest so that it can be replaced. The model is thus composed of two TRNSYS components: a control Type, and a heat pump Type.

The interface of the control component is quite simple; it only takes the return and setpoint temperatures as inputs, along with some control parameters, then outputs the compressor frequency. It is a little more complex for the heat pump component; its interface is detailed in fig. 5.1.

In his thesis, St-Onge [10] developed a performance map-based TRNSYS model for VCAAHPs in heating mode. Although it tackles some important issues such as defrost, there are aspects that could be improved, and features that are yet to be added. Those include

- a cooling operation mode,

- a dedicated control strategy,

- a dependency between defrost cycles and outdoor humidity.

Models aiming to simulate variable capacity VCAAHPs already exist, though they usually rely on performance curves instead of performance maps. For instance, the EnergyPlus variable refrigerant flow heat pump model [5, section 16.7.1] uses bi-quadratic curves to correct the capacity and input power according to the indoor and outdoor temperatures, but does not take the air flow rate or compressor frequency into account. Cheung and Braun propose a model involving the indoor humidity [15] and the air flow rate [16]. It uses single-variable regressions to correct rated values, similarly to the approach presented in chapter 4. However, it does not take the frequency as input, rather it features three modes with minimum capacity, maximum capacity and part load. Gayeski et al. developed a model for cooling mode [17] where the total capacity and the input power are computed using a

3$^{\text{rd}}$ degree polynomial with 25 terms determined experimentally. It depends on the indoor and outdoor temperatures, the compressor frequency, and the condenser fan speed (which, in cooling mode, is *not* that of the indoor unit). In addition, sensible and latent capacities are not evaluated, and there is no dependency on the humidity.

The frequency seems to be systematically excluded from the *air-source* heat pump model inputs, supposedly because of the complexity arising when many variables are involved. It is more common to find a frequency input in *ground-source* heat pump models, for which some aspects that hard are to model—such as defrost—do not have to be considered. Madani et al. developed a TRNSYS model taking the frequency into account [18], but that does not cover defrost operation or sensible/latent ratios in cooling mode. Another TRNSYS model using performance maps instead of performance curves was developed by Bouheret and Bernier [19] for water-to-air ground-source heat pumps. With this approach, manufacturer data can be used more easily, and there is more flexibility regarding the relation between the performance and the input variables. The model includes the frequency in its inputs, however it is not an entry but rather an output of the performance map, depending on the heat pump capacity. Therefore, the capacity is determined using a linear regression of the form $af_c + b$, where a and b are determined from the operating conditions. According to the authors, "It would have been preferable to have performance maps with capacity given as a function of frequency."

5.1 Controller

The goal of the controller component is to compute the value of the four control variables defined in chapter 3, i.e., the compressor frequency, the operating mode, the air flow rate, and the defrost mode.

To compute the compressor frequency, the controller implements the PI control strategy of section 3.1.1 and the frequency saturation and quantization described in sections 3.1.2 and 3.1.3. Because of the frequency limitations, there is also an anti-windup feedback loop (fig. 5.2) with a tracking time constant τ_t to desaturate the integral when the limits are exceeded, following the method explained by Wittenmark et al. [20].

The operating mode γ is implemented as described in section 3.2.

5.2 Heat pump

Whenever the value of at least one of the performance map input quantities mentioned in chapter 2 is not in the performance map entries, the heat pump component must perform

return air temperature $\quad T_r$
return temperature setpoint $\quad T_{\text{set}}$

control
file

controller $\qquad f_{\text{c}}$ compressor
frequency

return air temperature $\quad T_r$
return air humidity ratio $\quad \omega_r$
return air pressure $\quad p_r$

outdoor air temperature $\quad T_o$
outdoor air humidity ratio $\quad \omega_o$
outdoor air pressure $\quad p_o$

heat
pump

indoor unit fan power draw $\quad P_{\text{fi}}$
outdoor unit fan power draw $\quad P_{\text{fo}}$
indoor unit mass flow rate $\quad \dot{m}_{\text{a}}$

performance
map

supply air temperature $\quad T_s$
supply air humidity ratio $\quad \omega_s$

heating rate $\quad \dot{Q}_{\text{h}}$
cooling rate $\quad \dot{Q}_{\text{c}}$
total power draw $\quad P_{\text{el}}$
compressor power draw $\quad P_{\text{comp}}$
coefficient of performance $\quad$ COP

Figure 5.1: The control part is separated from the rest of the model.
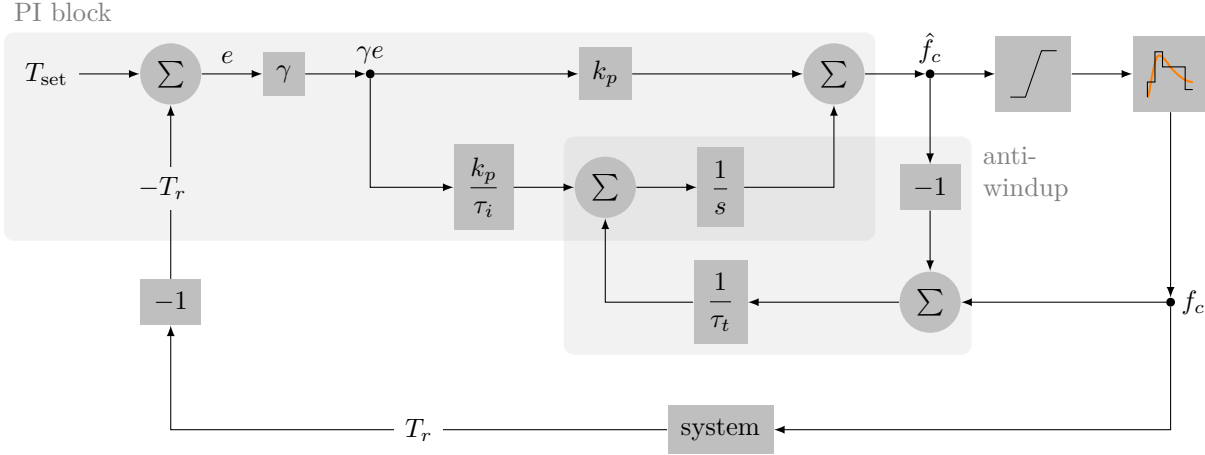
Figure 5.2: The return air temperature control is composed of a PI block, a saturater, a quantizer, and an anti-windup.

an interpolation to obtain more accurate performance values. Interpolation with only one variable is rather straightforward, but it gets more complicated as the number of variables increases. Additionally, several multivariate interpolation methods exist. Here, the piecewise multilinear interpolation is used.

Once the performance values are interpolated from the table, the heat pump component uses those values to determine the supply air state.

5.2.1 Interpolation

The interpolation approach followed by several TRNSYS components relying on interpolation, as well as St-Onge's model [10], is to use a standard function from the TRNSYS kernel to read the required values in the performance file at each timestep. Although convenient from the programming point of view, it has two drawbacks. First, it requires to open the file, skim through a potentially high number of lines to read the values, then close the file at each timestep—which is not really efficient regarding the computational effort. Second, it must know beforehand the number of entries in the table for each variable, which means that the user has to specify all of them as parameters of the model; this causes the model interface to be not very user friendly. Another approach is thus used for the model: the whole performance map is read entirely once at the very beginning of the simulation and then stored as a contiguous array. It can then be accessed in a much more efficient way in subsequent timesteps, and users don't have to bother with entering the performance map dimensions in the TRNSYS project.

However, this implies that the code reading the performance map needs to be rewritten. On the plus side, one can control how the values are read and, especially, check more easily that the provided values are coherent.

The goal is to find, given a set of $N = 5$ input variables[1] $\mathbf{v} = (T_r, T_o, T_{\mathrm{wb}r}, \dot{V}_a^*, \nu)$, an approximation $\tilde{\mathbf{P}}(\mathbf{v})$ of the actual performance values $\mathbf{P}(\mathbf{v})$, where $\mathbf{P} = (P_{\mathrm{el}}, \dot{Q}_{\mathrm{h}})$ in heating mode and $\mathbf{P} = (P_{\mathrm{el}}, \dot{Q}_{\mathrm{cs}}, \dot{Q}_{\mathrm{cl}})$ in cooling mode ($\dot{V}_a^*$ denotes the normalized air flow rate). The approximation is computed from tables values of $\mathbf{P}$. The tables have *entries* in the form of a set $\mathbb{E} \subset \mathbb{R}^N$ with cardinality $|\mathbb{E}| = \prod_{i=1}^N n_i$ given by[2]

$$\mathbb{E} = \mathbb{T}_r \times \mathbb{T}_o \times \mathbb{T}_{\mathrm{wb}r} \times \dot{\mathbb{V}}_a \times \mathbb{F}_c$$

where

$$\mathbb{T}_r = \{\, T_{ri} \mid T_{ri} < T_{ri+1} \wedge i = 1, \ldots, n_1 \,\}$$
$$\mathbb{T}_o = \{\, T_{oj} \mid T_{oj} < T_{oj+1} \wedge j = 1, \ldots, n_2 \,\}$$
$$\mathbb{T}_{\mathrm{wb}r} = \{\, T_{\mathrm{wb}rk} \mid T_{\mathrm{wb}rk} < T_{\mathrm{wb}rk+1} \wedge k = 1, \ldots, n_3 \,\}$$
$$\dot{\mathbb{V}}_a = \{\, \dot{V}_{al}^* \mid \dot{V}_{al}^* < \dot{V}_{al+1}^* \wedge l = 1, \ldots, n_4 \,\}$$
$$\mathbb{F}_c = \{\, \nu_m \mid \nu_m < \nu_{m+1} \wedge m = 1, \ldots, n_5 \,\}$$

Each table's values are thus components of the tensors $T_{ijklm}^{\mathrm{el}} = P_{\mathrm{el}}(T_{ri}, T_{oj}, T_{\mathrm{wb}rk}, \dot{V}_{al}^*, \nu_m)$, and $T_{ijklm}^{\mathrm{h}} = \dot{Q}_{\mathrm{h}}(T_{ri}, T_{oj}, T_{\mathrm{wb}rk}, \dot{V}_{al}^*, \nu_m)$. Both $\mathbf{T}^{\mathrm{el}}$ and $\mathbf{T}^{\mathrm{h}}$ are elements of $\prod_{i=1}^N \mathbb{R}^{n_i}$.

Given that $\mathbf{v}$ is usually not an element of $\mathbb{E}$ (i.e. it is not a entry of the tables), $\tilde{\mathbf{P}}(\mathbf{v})$ is computed from a subset $\{\, \mathbf{v}_\lambda \mid \lambda = 1, \ldots, \Lambda \,\} \subset \mathbb{E}$ such that elements $\mathbf{v}_\lambda$ are bounding $\mathbf{v}$. There are several possible combinations; in particular, Weiser and Zarantonello [21] presented two interpolation methods where the elements $\mathbf{v}_\lambda$ form a N-box or a N-simplex (see fig. 5.3); the methods are respectively called piecewise multilinear interpolation and piecewise linear interpolation. The piecewise linear interpolation is found to be more efficient because it only needs to locate the right simplex by sorting N numbers and then perform N operations, while the piecewise multilinear interpolation needs to perform 2^N operations. Moreover, the required number of points for the interpolation Λ is smaller, especially when N grows: $\Lambda = N + 1$ for the N-simplex, and $\Lambda = 2^N$ for the N-box.

However, as opposed to a conclusion from Weiser and Zarantonello, the two methods do *not*

---

[1]In this section, only the variables for the cooling mode operation are used, to avoid unnecessary redundancy. All the concepts are easily adapted to heating mode, for which $N = 4$ and $\mathbf{v} = (T_r, T_o, \dot{V}_a^*, \nu)$.

[2]With this number of variables, it can be a little hard to visualize things; a more illustrated description of the performance map is provided in fig. 4.1.
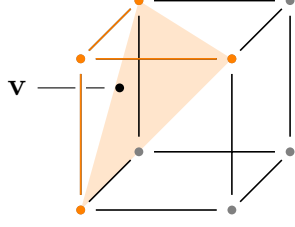
Figure 5.3: The input values vector $\mathbf{v} \in \mathbb{R}^3$ can be bound by a 3-box ($\Lambda = 8$), or by a 3-simplex ($\Lambda = 4$).

have a similar accuracy considering typical performance map entries. This stems from the relatively sparse performance map structure: the n_i values typically range from 3 to 10, while the entries have to cover a range of operating conditions that can be quite large. Additionally, at $N = 5$, using a simplex instead of a box means using the information in 6 table values instead of 32, which amounts to a significant information loss if the entries grid is not dense enough. In this case, the N-box boundary is thus preferred for the interpolation.

The first step in the interpolation is thus to find the set of vertices $\mathbb{V} = \{\, \mathbf{v}_\lambda \,\}$ of this N-box. The vertices are found from those values η_κ, $\kappa = 1, \ldots, N$ such that

$$T_{r\,\eta_1} \leq T_r \leq T_{r\,\eta_1+1}$$
$$T_{o\,\eta_2} \leq T_o \leq T_{o\,\eta_2+1}$$
$$T_{\text{wbr}\,\eta_3} \leq T_{\text{wbr}} \leq T_{\text{wbr}\,\eta_3+1}$$
$$\dot{V}^*_{a\,\eta_4} \leq \dot{V}^*_a \leq \dot{V}^*_{a\,\eta_4+1}$$
$$\nu_{\eta_5} \leq \nu \leq \nu_{\eta_5+1}$$

wich yields

$$\mathbb{V} = \{\, T_{r\,\eta_1}, T_{r\,\eta_1+1} \,\} \times \{\, T_{o\,\eta_2}, T_{o\,\eta_2+1} \,\} \times \{\, T_{\text{wbr}\,\eta_3}, T_{\text{wbr}\,\eta_3+1} \,\} \times \{\, \dot{V}^*_{a\,\eta_4}, \dot{V}^*_{a\,\eta_4+1} \,\} \times \{\, \nu_{\eta_5}, \nu_{\eta_5+1} \,\}$$

The input values $\mathbf{v}$ can then be scaled to values $\mathbf{u}$ bound by the unit N-cube (see fig. 5.4):

$$u_\kappa = \frac{v_\kappa - v_{\kappa\eta_\kappa}}{v_{\kappa\eta_\kappa+1} - v_{\kappa\eta_\kappa}} \qquad \kappa = 1, \ldots, N$$

Finally, defining $\mathbf{R}(\mathbf{u}) \triangleq \tilde{\mathbf{P}}(\mathbf{v}(\mathbf{u}))$ with $v_\kappa(u_\kappa) = v_{\kappa\eta_\kappa} + u_\kappa(v_{\kappa\eta_\kappa+1} - v_{\kappa\eta_\kappa})$, and $\alpha_\kappa \in \{0,1\}$, the approximation is computed recursively:

$$\tilde{\mathbf{P}}(\mathbf{v}) = \mathbf{R}(u_1, \ldots, u_N) = (1 - u_1)\,\mathbf{R}(0, u_2, \ldots, u_N) + u_1\,\mathbf{R}(1, u_2, \ldots, u_N)$$
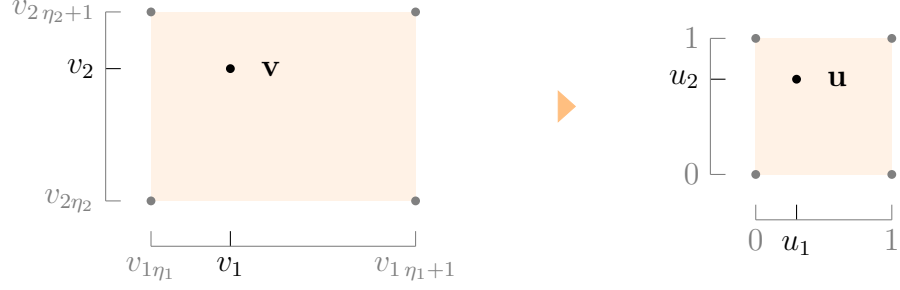
Figure 5.4: The input values $\mathbf{v} = (v_1, v_2)$ are scaled to values $\mathbf{u} = (u_1, u_2)$ within the unit square.

where $\mathbf{R}(0, u_2, \ldots, u_N)$ and $\mathbf{R}(1, u_2, \ldots, u_N)$ are computed the same way, following the rule

$$
\mathbf{R}(\alpha_1, \ldots, \alpha_{\kappa-1}, u_\kappa, \ldots, u_N) = (1 - u_\kappa) \, \mathbf{R}(\alpha_1, \ldots, \alpha_{\kappa-1}, 0, u_{\kappa+1}, \ldots, u_N)
$$
$$
+ u_\kappa \, \mathbf{R}(\alpha_1, \ldots, \alpha_{\kappa-1}, 1, u_{\kappa+1}, \ldots, u_N)
$$

The 2^N base cases $\mathbf{R}(\alpha_1, \ldots, \alpha_N)$ are the table values associated with the 2^N vertices in $\mathbb{V}$.

5.2.2 Supply air state

Once the capacity is known from the interpolation, the supply air state can be determined. It is rather straightforward in heating mode, since the amount of water vapour in the air does not change, i.e. $\omega_s = \omega_r$. In cooling mode however, since the air is cooled there may be condensation, thereby decreasing the supply air humidity content (see fig. 5.5). The amount of condensed vapour is determined by the latent cooling capacity $\dot{Q}_{\text{cl}}$.

With the return air pressure and temperature provided as inputs, the return air density ρ_r

(a) Heating mode

(b) Cooling mode, with condensation
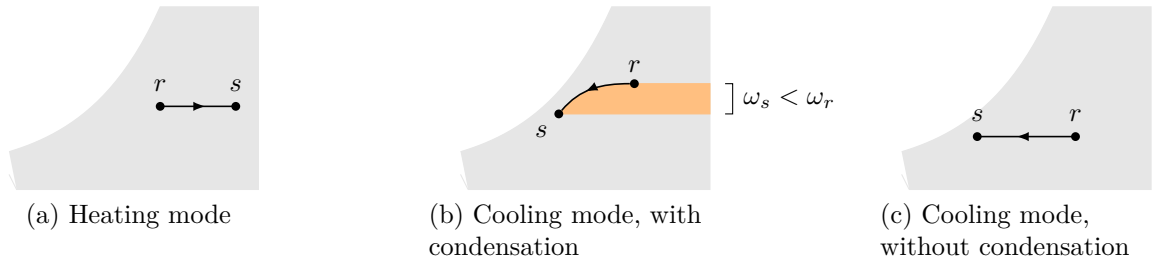
(c) Cooling mode, without condensation

Figure 5.5: There may be a decrease in humidity content when operating in cooling mode, depending on the return air humidity. This does not happen in heating mode since the relative humidity decreases.

can be obtained, and thus also the air mass flow rate: $\dot{m}_a = \rho_r \dot{V}_a$. In heating mode, the supply air state is obtained from the quantities

$$h_s = h_r + \frac{\dot{Q}_h}{\dot{m}_a}$$

$$\omega_s = \omega_r$$

$$p_s = p_r \qquad \text{(fan pressure drop neglected)}$$

In cooling mode, computing the supply humidity ratio requires to define an intermediate state x such that $\omega_x = \omega_s$ and $T_x = T_r$ (fig. 5.6). With the temperature known, the state x is then determined by

$$h_x = h_r - \frac{\dot{Q}_{cl}}{\dot{m}_a}$$

$$p_x = p_r$$

and the supply air state by

$$h_s = h_r - \frac{\dot{Q}_{cs} + \dot{Q}_{cl}}{\dot{m}_a}$$

$$\omega_s = \omega_x(h_x, p_x, T_x)$$

$$p_s = p_r$$

Finally, the condensate air mass flow rate is $\dot{m}_w = \dot{m}_a(\omega_r - \omega_s)$.
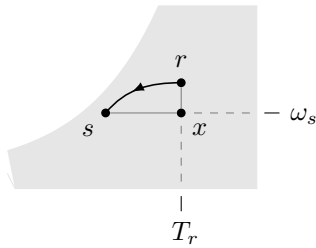
Figure 5.6: When there is latent heat, the supply air state is determined through an intermediate state x.

5.3   Simulation results

Three types of simulation are presented in this section, both in heating and in cooling mode. First, the heat pump component is tested alone, without the controller component. Then, it is tested with the controller in a minimal working example. Finally, a case study is presented, where the model is used in a simulation with a typical residential unit of a duplex or triplex.

5.3.1 Heat pump component

In order to test the heat pump component independently from the controller, the inputs that would normally come from other components in the simulation—such as the return temperature or the compressor frequency—are read from a file containing measurements. The component outputs—basically the interpolation results and the supply air state—can then be compared to the corresponding measured quantities.

The heat pump component is able to accurately reproduce the performance values and heating supply air state from the measured environmental conditions and frequency values (figs. 5.7 and 5.8). The humidity sensors, being quite sensitive to variation and, in the case of ϕ_s, located in an air flow that is strongly fluctuating, introduce noise in many other quantities, including $\dot{Q}_{cs}$ and $\dot{Q}_{cl}$ since they are obtained from the SHR values. This also explains why there is a spread so wide in SHR measurements of fig. 4.10. Since the supply temperature and humidity are calculated by the model based on the (noisy) latent and sensible loads, they are also relatively noisy but their average value seem close to the measured supply conditions (around $14\,°C$ and $65\,\%$ humidity).
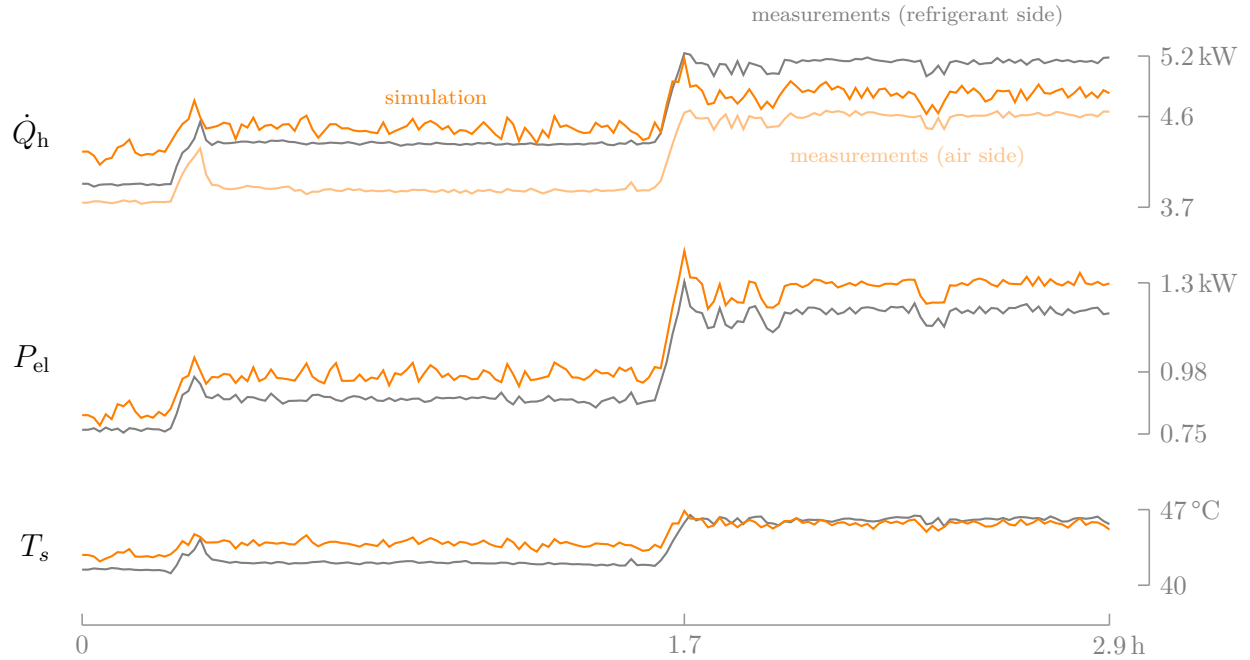
Figure 5.7: At the selected heating rated conditions, but with a frequency $\nu = 0.5$ for $t < 1.7\,h$ and $\nu = 0.59$ for $t > 1.7\,h$, the performance and supply air state seem well approximated by the model; this supports the validity of the correlations $\varphi_{h1}(\nu)$ and $\varphi_{h2}(\nu)$.
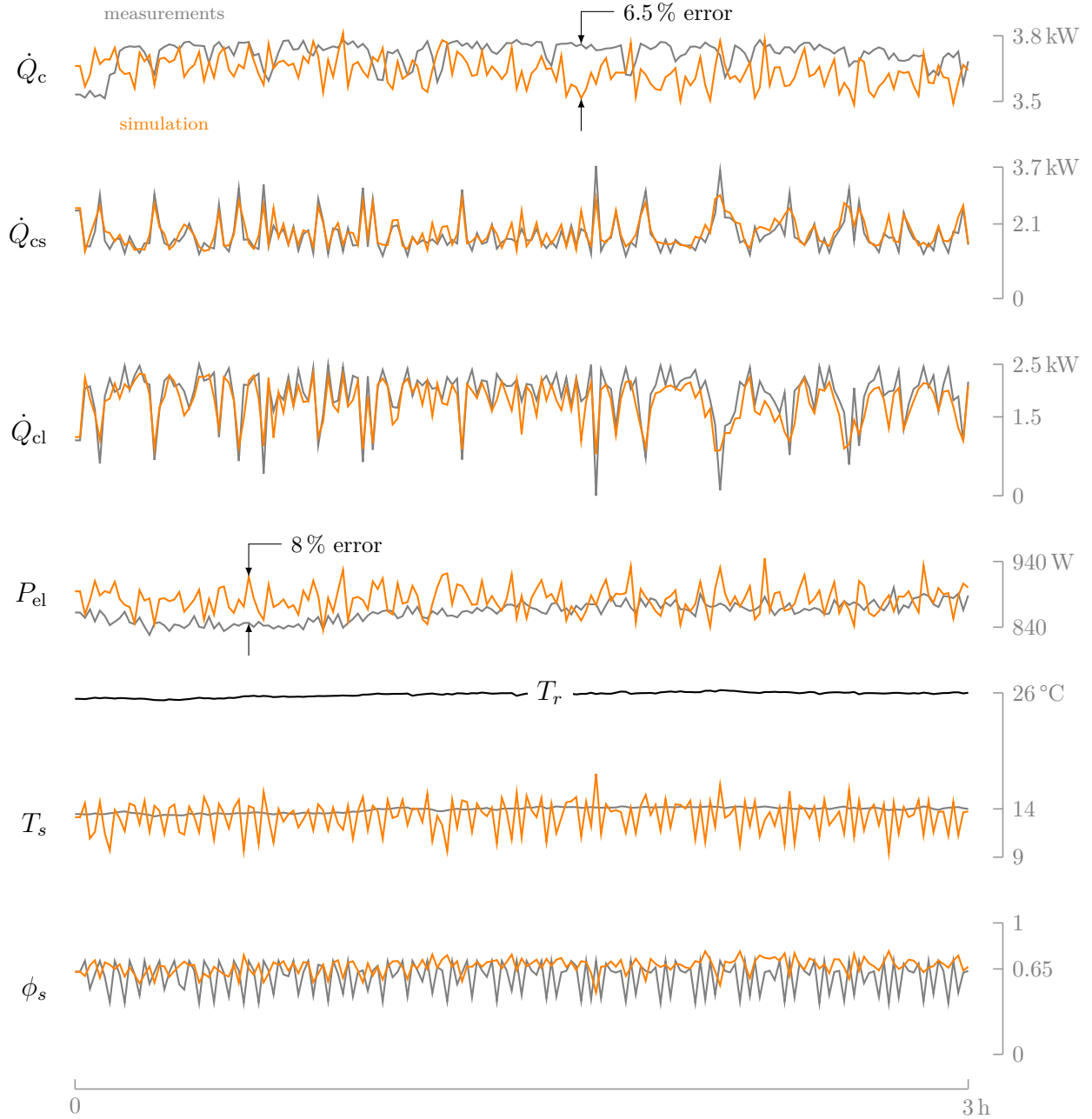
Figure 5.8: Both the total capacity and the input power are quite well approximated at conditions close to the rated ones ($T_o = 41\,°C$ and $f_c = 54\,Hz \Leftrightarrow \nu = 0.95$). Only the humidity is significantly different from its rated value ($\overline{\phi}_r = 55.2\,\%$ against $6\,\%$ in rated conditions), which means that the humidity has little influence on the total capacity. Sensible and latent capacities sometimes have differences a little bit larger due to the noise on humidity values, but they are still quite a good match.

5.3.2 Whole model (controller and heat pump)

To test the model as a whole (controller and heat pump), since there is a feedback loop the simulation must include a model for the thermal response of the room being heated or cooled—this corresponds to the *system* block in fig. 5.2. The Type 88 implementing a simple lumped capacitance model is used for that purpose.

The defrost cycles simulated by the controller seem to occur at a similar frequency than those measured, although not being perfectly synced (fig. 5.9). After the defrost, the capacity is increasing slowly because of the recovery penalty, causing the compressor to operate at full speed. Once the recovery period is close to an end, the capacity reaches a peak until the temperature returns to the setpoint, then decrease suddenly to reach a steady-state value until the next defrost. The measured capacity on the other hand increases suddenly just after the defrost and then very slowly until a new cycle begins. This seems rather different than the PI control behaviour of the model, but the capacity levels are similar.

In contrast, power draws, following the frequency variations, are very different. The simulated power reaches higher levels then drops abruptly, whereas the measured power is more steady.

As in fig. 3.14, the measured indoor temperature drops very quickly when defrost begins because the load is imposed by changing the air using the indoor shed fan, so there is very little inertia. The outdoor temperature is not constant either because, in defrost mode, heat is rejected from the outdoor unit instead of absorbed by it. The quick change of indoor and outdoor conditions in response to a defrost cycle is representative of the testing environment but not of a real situation, where internal mass would dampen the indoor temperature response and where the heat pump would have no impact on the outdoor conditions.

Discrepancies are also present in the cooling operation, but there is a good match in the dynamic behaviour—except for the fast cycling at startup. This is an example of undocumented behaviour whose cause and purpose are not easy to establish, hence it would be difficult to integrate it in the model. Apart from that, simulated sensible and latent capacities are not affected by noise anymore since the they do not rely on humidity measurements.

In the last quarter of the cooling operation, the simulated quantities catch up to the measurements and enter steady-state. Overall, they seem to respond more slowly than the measured quantities, but this does not affect the indoor temperature.

All in all, the average behaviour of the model is similar, with some differences with the dynamic behaviour. The model includes some high-level mechanisms such as frequency limits and defrost cycles. However, for the model to be able to adequately simulate a variety of VCAAHPs, it cannot go too far in replicating the operation details of a particular heat pump.
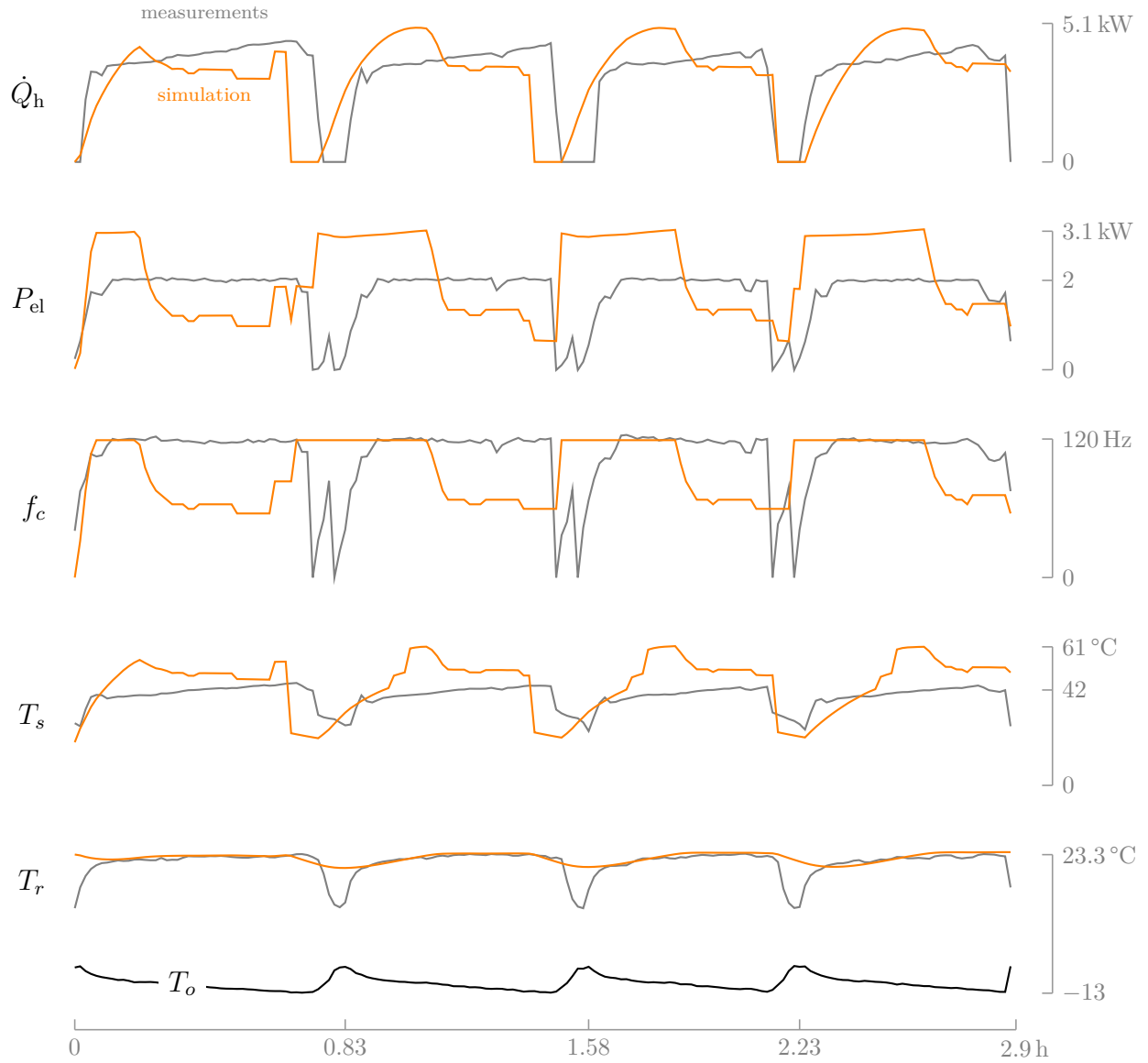
Figure 5.9: The simulated defrost cycles occur at a frequency similar to the measured ones.
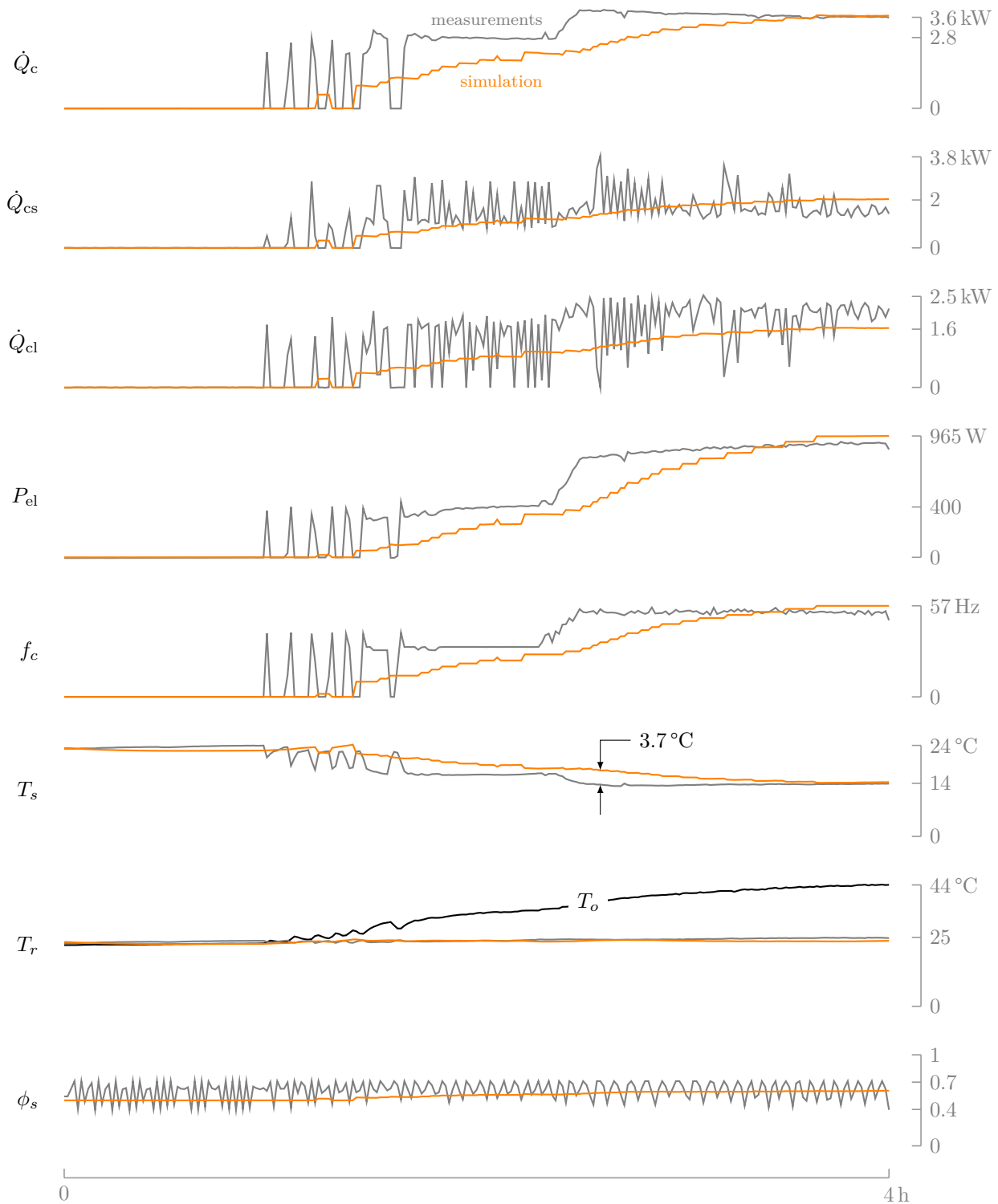
Figure 5.10: The model is a little slower in bringing its values into steady-state. Nonetheless, the overall behaviour of the heat pump is well approximated. Once steady-state is reached, measured and simulated values are very close.

5.3.3 Case study: implementing a VCAAHP in a residential unit

The modelled building is a single unit of a duplex or triplex. The top unit is modelled, and identical boundary conditions are assumed for units next to and below the modelled one. The unit has a floor area of $72\,\mathrm{m^2}$ and represents an average existing building, with moderate insulation (wall $R_{\mathrm{SI}} = 1.7\,\mathrm{m^2\,K\,W^{-1}}$, roof $R_{\mathrm{SI}} = 3.2\,\mathrm{m^2\,K\,W^{-1}}$, respectively $R10$ and $R18$ in $\mathrm{ft^2\,{}^\circ F\,h\,Btu^{-1}}$). The window-to-wall ratio is $30\,\%$ for the front facade (shown in fig. 5.11, which is assumed to face due south) and $22\,\%$ for the back facade, including glazed doors to balconies. The overall U value (including framing) is approximately $3\,\mathrm{W\,m^{-2}\,K^{-1}}$ for windows and $3.5\,\mathrm{W\,m^{-2}\,K^{-1}}$ for doors. The envelope is relatively leaky ($ACH_{50} = 6\,\mathrm{h^{-1}}$); the Sherman-Grimsrud model is used to model infiltration, assuming a leakage area at $4\,\mathrm{Pa}$ $ELA_4 = 270\,\mathrm{cm^2}$ and local shelter class $= 5$ (dense urban).

The unit is assumed to be occupied by 2 people. Internal gains and occupancy schedules are adapted and scaled down from typical Canadian schedules used at the Canadian Centre for Housing Technology facility [22]. This profile only contains a single day type, so there are no differences between weekdays and weekends.

The simulation uses a typical weather data file for the McTavish station in Montréal [23]. A reference simulation with constant setpoints ($22\,{}^\circ\mathrm{C}$ for heating and $26\,{}^\circ\mathrm{C}$ for cooling) and an idealized HVAC system results in a yearly energy use of $4540\,\mathrm{kWh}$ for heating (COP $= 1$) and $655\,\mathrm{kWh}$ for cooling (COP $= 2.5$)—note that the simulation does not account for natural ventilation through open windows.

The VCAAHP simulation uses a $1\,\mathrm{min}$ time step.
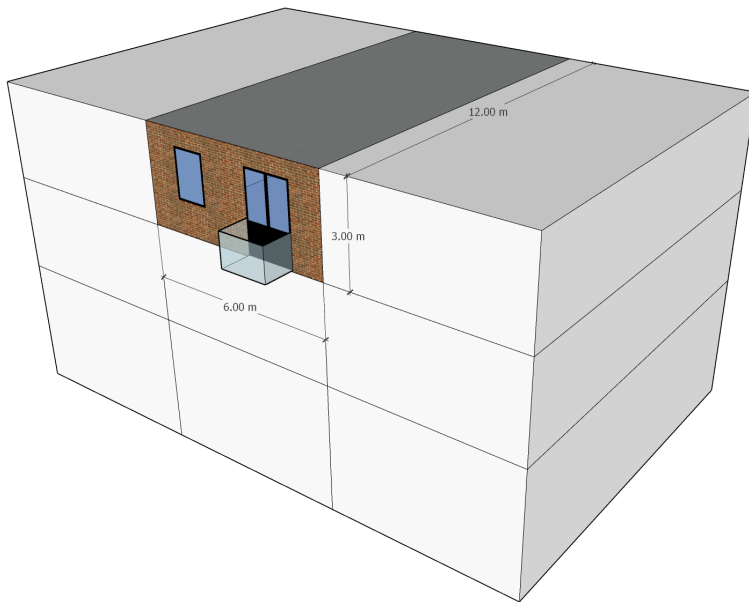
Figure 5.11: Modelled housing unit. The whole assembly is depicted in fig. 5.15.

Figure 5.12 shows two selected days in cooling. The first day is relatively mild, and cooling is only required around noon. The machine operates mostly under the PID algorithm with a quantized output, and the room temperature is maintained within a few tenths of a degree of the setpoint, even after a sudden increase in internal gains at 5 PM. At the end of the day, the machine performs a few on-off cycles due to the very low load. The next day is warmer, and cooling starts around 7:15 AM with a relatively high latent load, as the outside air is relatively humid and there was very little dehumidification on the previous day. The machine then modulates its frequency to maintain the temperature within a few tenths of a degree of the setpoint.
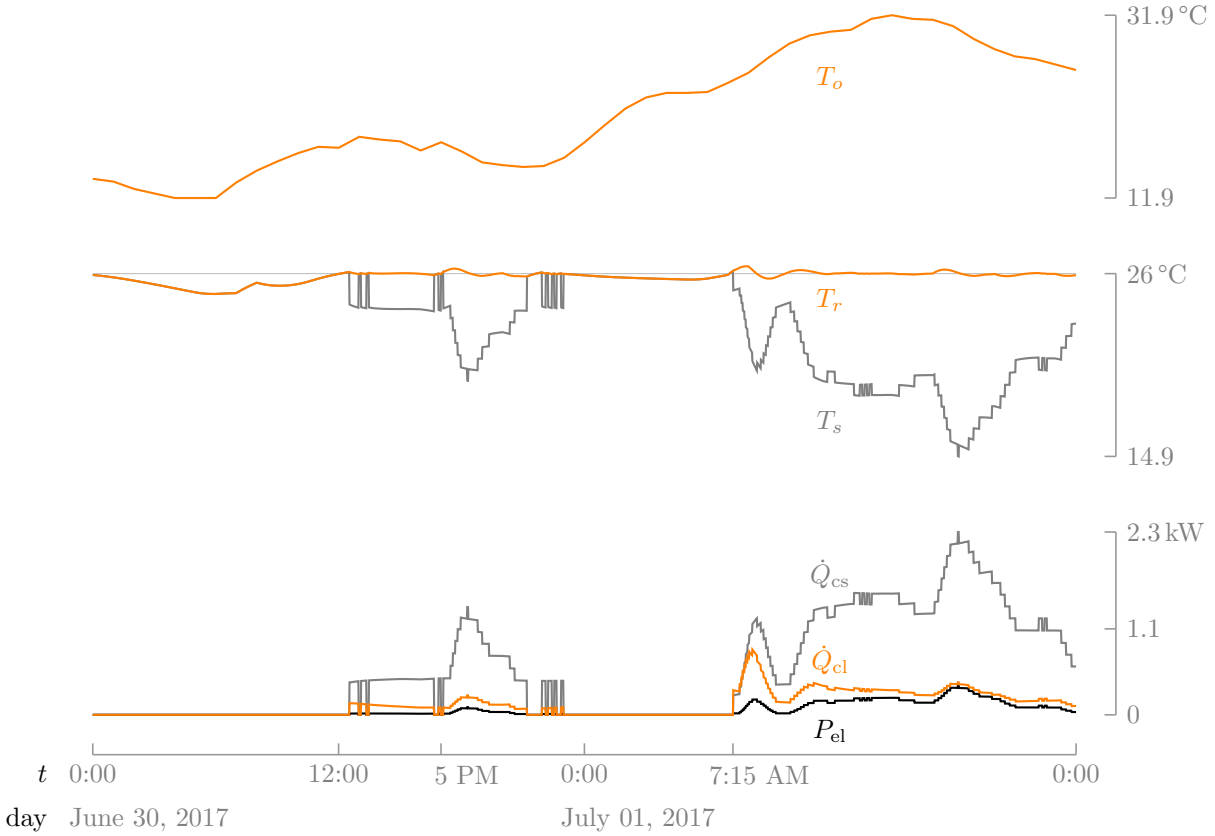
Figure 5.12: Example of operation during the cooling season.

Figure 5.13 shows two selected days in heating. The first day is relatively mild. The heat pump modulates its frequency to match the load, and the temperature is kept virtually at the setpoint. There are no defrost cycles. The ambient temperature drops quickly during the afternoon, and the second day is much colder. Heating is not required during the afternoon because solar gains are high, but heating starts around 8 PM. Defrost cycles are visible in the plots, with the heating power dropping to zero for a few minutes and then ramping up before reaching a steady state. The maximum frequency reached between defrost cycles is adjusted by the PID to meet the heating load.
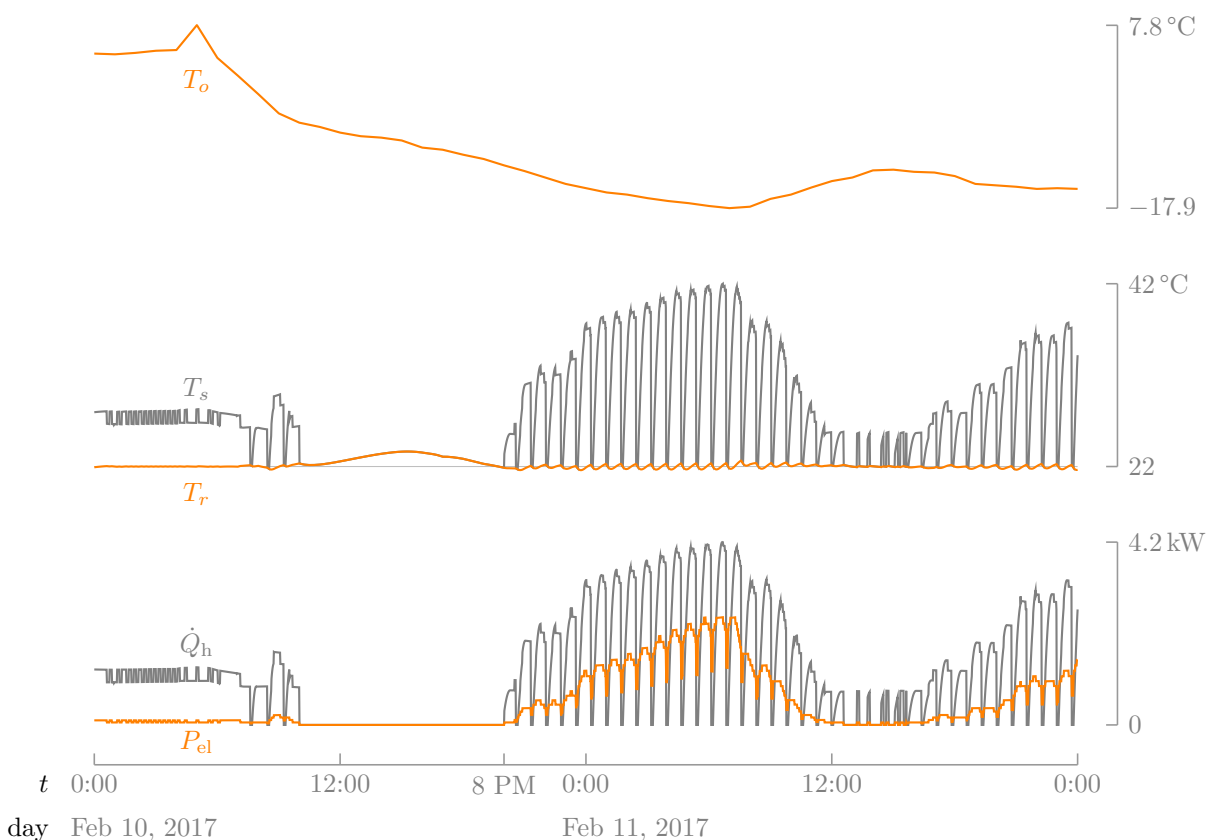
Figure 5.13: Example of operation during the heating season.

Figure 5.14 shows a detail of a period when several defrost cycles occur during otherwise relatively constant conditions. Defrost cycles are clearly visible, with a duration of about 5 minutes. The machine takes about 20 minutes to recover, and then the PID starts to modulate the frequency to limit the overshoot. The room temperature drops during the defrost periods as no heat is provided by the machine. The lowest temperature reached is about $0.6\,^\circ\text{C}$ lower than the setpoint. These excursions would be affected by internal thermal mass and are much lower than what was observed in the testing sheds (compare these results to the results from fig. 3.14).
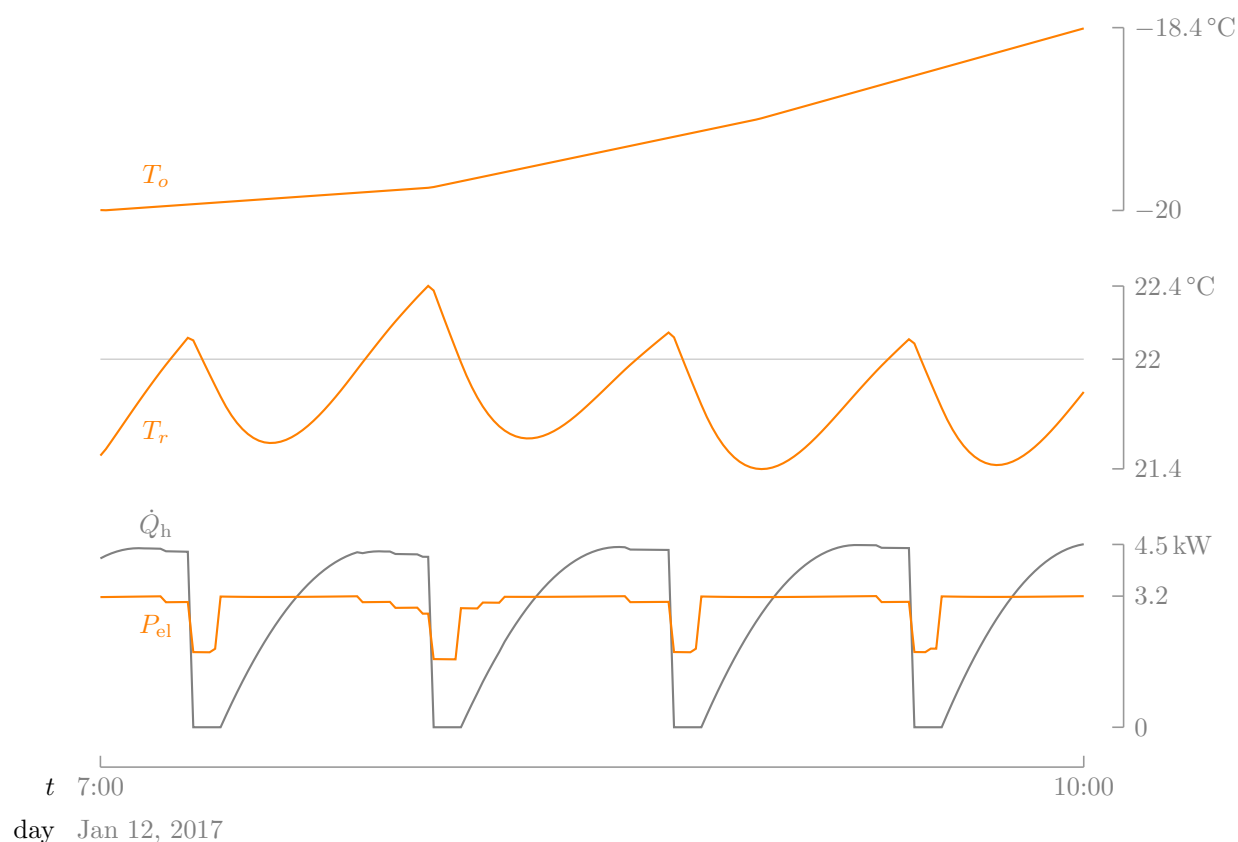
Figure 5.14: Detailed heating operation.
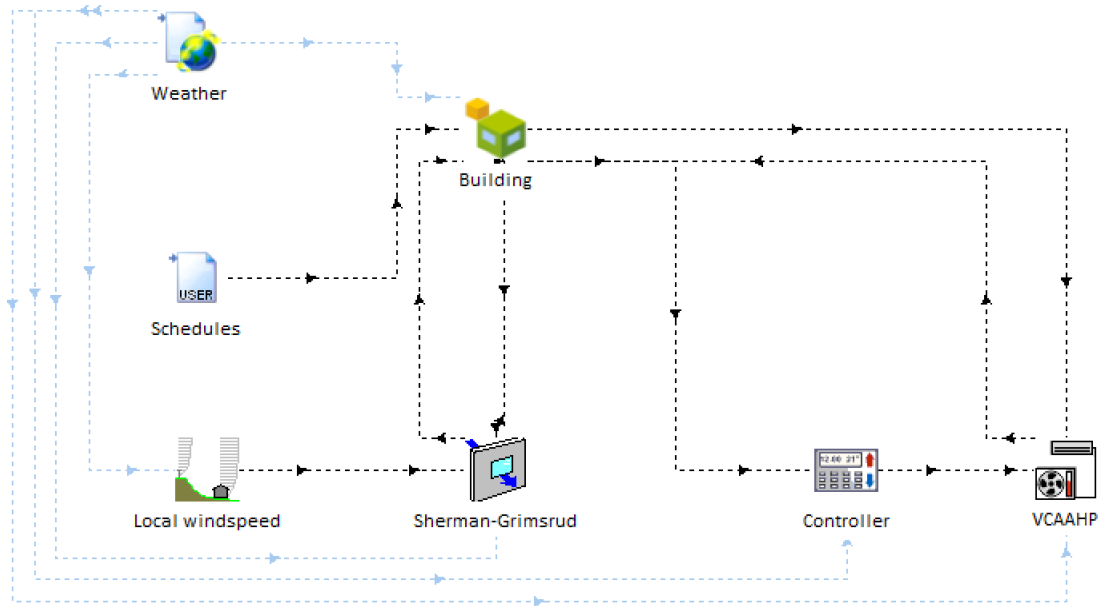
Figure 5.15: Besides the two components of the heat pump model, the TRNSYS assembly of the case study includes a detailed building model involving infiltration and user schedules, and a weather data file.

5.3.4 Summary

The heat pump component is able to correctly predict the performance and the supply air state if provided with the right inputs. The complete model with the controller loses a little bit of variability but is still able to correctly reproduce the main dynamic behaviours such as defrost. The VCAAHP model usability was demonstrated with a case study involving a detailed building model. Although the simulation results cannot be validated, a discussion of the results for some specific days highlighting different behaviours modelled by the heat pump showed that they make sense.

CHAPTER 6   CONCLUSION

To answer a need of integrating variable capacity heat pumps into HVAC simulations, a TRNSYS model was developed. For simplicity, a "black box" modelling approach based on performance maps was selected. To build these performance maps, experimental tests were conducted at the CanmetENERGY research centre in Varennes, QC. Control strategies were also analyzed and modelled based on a set of parameters collected in a formatted control file. A new interpolation method was proposed, with its associated performance map format. Regressions were deduced from experimental data so that any user can obtain a full performance map—and therefore use the model—from values typically provided by manufacturers. Finally, some simulation results were analyzed to validate the model, and a case study showed how the model behaves in actual simulations.

6.1   Summary of works

There are four main contributions to this project.

1. A TRNSYS model for VCAAHPs, including a dedicated controller implementing detailed control rules to select operation modes and adjust the compressor frequency. The code for both components is available on GitHub: `https://github.com/polymtl-bee/vcaahp-model`.

2. Experimental testing of a mini-split VCAAHP including cooling mode operation to validate and complement manufacturer data.

3. A set of regressions to fill missing values in performance maps as they are typically provided by manufacturer currently.

4. Simulations were performed to calibrate and check the proposed model against the experimental data. A case study coupling the VCAAHP with a detailed building model of a residential unit was then performed to demonstrate the model usefulness.

6.2   Limitations

Even though the heat pump has been tested in various conditions, some could not be reached due to control mechanisms, leaving gaps in the performance map. Missing data was supplemented by making assumptions, potentially reducing the accuracy.

Furthermore, many behaviours observed on the heat pumps still remain unclear. In particular, an unexpected cycling phenomenon occurs very frequently, even more so than steady-state operation.

Although a regression was provided to obtain the sensible heat ratio, two humidity dependencies are still missing. First, the influence of indoor humidity on cooling capacity and input power was found to be small—but still nonzero—and therefore neglected. Second, no relation was established between the defrost cycles parameters and the outdoor humidity.

Moreover, the dependency between the performance values and the indoor fan power could not be determined, so the air flow rate dependency remains unknown. One suspected cause of this problem is the low power level of the indoor fan, actually too low compared to the resolution of the power sensor. A *high* fan mode was therefore assumed, as it is the one at which manufacturer data are given.

Finally, the model is for now only valid for small timesteps, as the controller needs to be updated regularly for its outputs to make sense.

6.3   Future research

The first priority for future work would be to establish a regression between the different performance variables and the air flow rate, since it has a strong impact on performance.

To be able to perform experimental tests in every condition—especially frequency, which is not directly controlled—and get a more complete performance map, controls should, if possible, be overridden as advised in [24]. Tests with the heat pump internal control should still be conducted to establish an adequate control file.

Simulations over a long time period may require a large timestep (typically 1 h). A large timestep feature should therefore be implemented to run such simulations and approximate dynamic aspects such as defrost and boost frequency by "derated" performance curves.

Humidity dependency should be investigated in more detail. Finding a correlation between performance values and indoor humidity (and possibly other variables) would improve the steady-state accuracy of the model. Likewise, adding a dependency between defrost parameters and outdoor humidity would potentially improve the dynamic accuracy of the model.

To further improve modelling of defrost operation, the cooling performance map could be extended to lower temperature values, since during defrost the heat pump operates in cooling at low temperatures.

REFERENCES

[1] Natural Resources Canada, "Secondary Energy Use and GHG Emissions by End-Use in 2015-2016 for the Residential Sector," Ottawa, 2018. [Online]. Available: http://oee.nrcan.gc.ca/corporate/statistics/neud/dpa/showTable.cfm?type=CP&sector=res&juris=ca&rn=2&page=0.

[2] J. Winkler, "Laboratory Test Report for Fujitsu 12RLS and Mitsubishi FE12NA Mini-Split Heat Pumps," US Department of Energy, Tech. Rep., Oakridge, TN, USA, 2011.

[3] J. D. Munk, R. J. K., A. Odukomaiya, and A. C. Gehl, "Residential variable-capacity heat pumps sized to heating loads," 2014. [Online]. Available: https://www.osti.gov/biblio/1185392-residential-variable-capacity-heat-pumps-sized-heating-loads.

[4] M. Kegel, J. Sager, M. Thomas, D. Giguere, and R. Sunye, "Performance Testing of Cold Climate Air Source Heat Pumps," in *Proceedings of the 12th IEA Heat Pump Conference*, 15-18 May 2017.

[5] U.S. Department of Energy, *EnergyPlus Engineering Reference (v. 9.3.0)*, Washington, DC, USA, March 2020. [Online]. Available: https://energyplus.net/documentation

[6] I. H. Bell, J. Wronski, S. Quoilin, and V. Lemort, "Pure and pseudo-pure fluid thermophysical property evaluation and the open-source thermophysical property library CoolProp," *Industrial & Engineering Chemistry Research*, vol. 53, no. 6, pp. 2498–2508, 2014. [Online]. Available: http://pubs.acs.org/doi/abs/10.1021/ie4033999.

[7] M. Kegel and E. McDonald, "Cold Climate Ductless Split Heat Pump Preliminary Test Report," Natural Resources Canada, Tech. Rep., Varennes, QC, Canada, 2015.

[8] Fujitsu General Limited, *Service instruction*, 2012, model: ASU12RLS3.

[9] A. Saleh and M. Rosa, "Analysis of control strategies and simulation of heating systems using Simulink/Matlab potential," *Journal of Thermal Engineering*, vol. 2, no. 15, pp. 921–927, 2016.

[10] G. St-Onge, "Variable Capacity Mini-Split Air Source Heat Pump Model for TRNSYS," Master's thesis, École Polytechnique de Montréal, 2018.

[11] Y. A. Çengel and M. A. Boles, *Thermodynamics: An Engineering Approach.* New York: McGraw-Hill Education, 2015.

[12] S. N. Vukosavic, *Electrical Machines*, ser. Power Electronics and Power Systems. Springer-Verlag New York, 2013.

[13] American Society of Heating, Refrigerating and Air-Conditioning Engineers, "Standard Representation of Performance Simulation Data for HVAC&R and Other Facility Equipment," Atlanta, GA, USA, Standard 205, 2017.

[14] Mitsubishi Electric Corporation, *Outdoor unit service manual*, 2010, model: MUZ-FE12NA.

[15] H. Cheung and J. E. Braun, "Performance mapping for variable ductless heat pump systems in heating, cooling and defrost operation," in *Proceedings of the 14th International Refrigeration and Air Conditioning Conference*, no. 2289, Purdue, West Lafayette, IN, USA, 16-19 July 2012.

[16] ——, "Performance mapping for variable-speed ductless heat pump systems in heating and defrost operation," *HVAC&R Research*, vol. 20, no. 5, pp. 545–558, 2014. [Online]. Available: https://doi.org/10.1080/10789669.2014.917934

[17] N. Gayeski, T. Zakula, P. R. Armstrong, and L. Norford, "Empirical modeling of a rolling-piston compressor heat pump for predictive control in low-lift cooling," *ASHRAE Transactions*, vol. 116, no. 1, 2010.

[18] H. Madani, P. Lundqvist, and J. Claesson, "Variable capacity heat pump systems, modelling and simulation," in *Proceedings of the 9th IEA Heat Pump Conference*, Zürich, Switzerland, 20-22 May 2008.

[19] S. Bouheret and M. Bernier, "Modelling of a water-to-air variable capacity ground-source heat pump," *Journal of Building Performance Simulation*, vol. 11, no. 3, pp. 283–293, 2018. [Online]. Available: https://doi.org/10.1080/19401493.2017.1332686

[20] B. Wittenmark, K.-E. Årzén, and K. Åström, *Computer Control: An Overview*, ser. IFAC PROFESSIONAL BRIEF. International Federation of Automatic Control, 2002.

[21] A. Weiser and S. E. Zarantonello, "A note on piecewise linear and multilinear table interpolation in many dimensions," *Mathematics of Computation*, vol. 50, no. 181, pp. 189–196, 1988. [Online]. Available: https://www.ams.org/journals/mcom/1988-50-181/S0025-5718-1988-0917826-0/.

[22] M. C. Swinton, H. Moussa, and R. G. Marchand, "Commissioning twin houses for assessing the performance of energy conserving technologies," in *Proceedings for Performance*

of Exterior Envelopes of Whole Buildings VIII: Integration of Building Envelopes, Clearwater Beach, FL, USA, 2-7 Dec 2001, pp. 1–10.

[23] R. Morris, "Final Report Updating CWEEDS Weather Files," Environment and Climate Change Canada, Toronto, ON, CAN, Tech. Rep., 2016.

[24] Air-Conditioning, Heating & Refrigeration Institute (AHRI), "Performance rating of unitary air-conditioning & air-source heat pump equipment," Arlington, VA, USA, Standard 210/240, 2017.
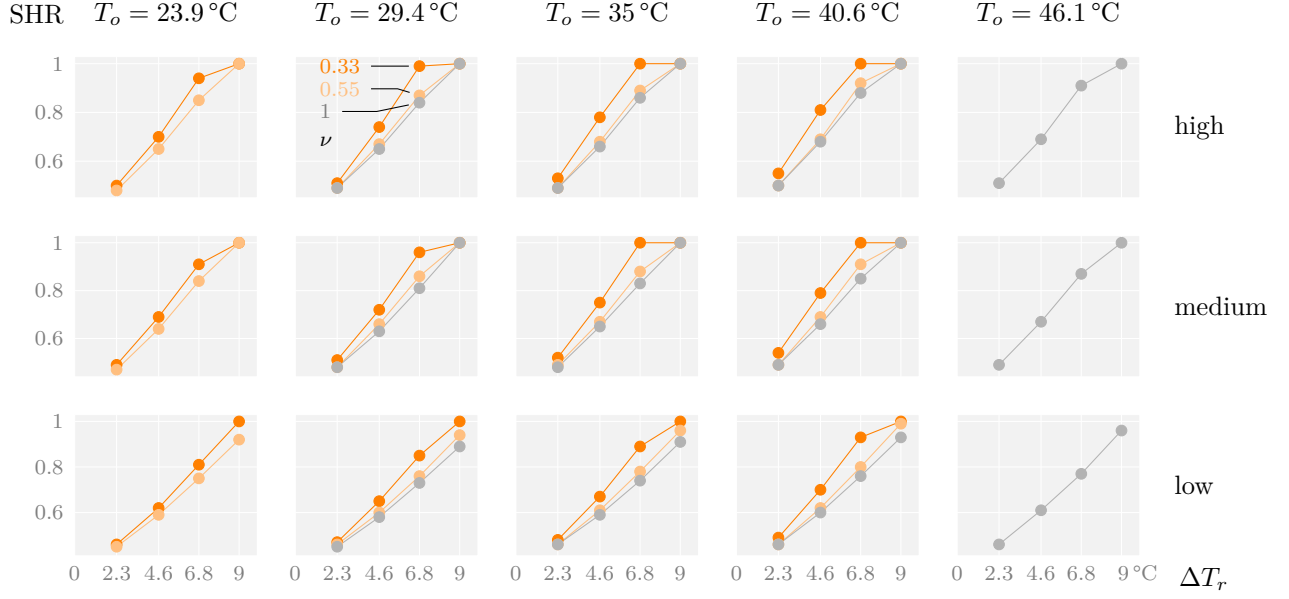
APPENDIX A   ASHRAE STANDARD 205 EXAMPLE DATA

Figure A.1: The SHR values from the ASHRAE 205 standard example data [13] globally increase with the wet-bulb depression and saturates around $\Delta T_r = 6.8\,°\text{C}$ in some conditions.

APPENDIX B   MANUFACTURER DATA FOR THE TESTED HEAT PUMP IN COOLING MODE

Table B.1: Example of manufacturer data—adapted from [8]. Values are given in kW, for an indoor air flow rate $\dot{V}_a = 0.23\,\mathrm{m^3\,s^{-1}}$.

| $T_r/°C$ | 17.8 | | | 21.1 | | | 23.9 | | | 26.7 | | | 29.4 | | | 32.2 | | |
| $T_{\mathrm{wb,r}}/°C$ | 12.2 | | | 15.6 | | | 17.2 | | | 19.4 | | | 21.7 | | | 22.8 | | |
$T_o/°C$	$\dot{Q}_\mathrm{c}$	$\dot{Q}_\mathrm{cs}$	P_el	$\dot{Q}_\mathrm{c}$	$\dot{Q}_\mathrm{cs}$	P_el	$\dot{Q}_\mathrm{c}$	$\dot{Q}_\mathrm{cs}$	P_el	$\dot{Q}_\mathrm{c}$	$\dot{Q}_\mathrm{cs}$	P_el	$\dot{Q}_\mathrm{c}$	$\dot{Q}_\mathrm{cs}$	P_el	$\dot{Q}_\mathrm{c}$	$\dot{Q}_\mathrm{cs}$	P_el
−10	3.03	2.79	0.28	3.38	2.81	0.28	3.73	3.07	0.29	3.84	3.31	0.29	4.07	3.29	0.29	4.3	3.5	0.3
−5	3.01	2.77	0.33	3.35	2.78	0.33	3.7	3.03	0.35	3.81	3.28	0.34	4.04	3.26	0.34	4.27	3.47	0.35
0	2.98	2.74	0.36	3.33	2.75	0.36	3.67	3.01	0.38	3.78	3.25	0.37	4.01	3.23	0.38	4.23	3.45	0.39
5	2.96	2.73	0.39	3.3	2.75	0.39	3.64	2.99	0.41	3.75	3.23	0.4	3.98	3.22	0.4	4.2	3.42	0.41
10	2.94	2.7	0.4	3.28	2.71	0.4	3.61	2.96	0.42	3.73	3.2	0.41	3.95	3.18	0.41	4.17	3.4	0.42
15	2.92	2.68	0.41	3.25	2.71	0.41	3.58	2.94	0.44	3.7	3.18	0.42	3.92	3.17	0.43	4.14	3.37	0.44
19.4	3.29	3.03	0.54	3.67	3.05	0.55	4.04	3.32	0.55	4.17	3.59	0.56	4.42	3.57	0.56	4.67	3.8	0.57
25	3.13	2.88	0.62	3.49	2.89	0.63	3.85	3.15	0.64	3.97	3.41	0.64	4.2	3.39	0.64	4.44	3.61	0.65
30.6	2.96	2.72	0.69	3.3	2.73	0.7	3.64	2.98	0.71	3.75	3.22	0.71	3.98	3.21	0.72	4.2	3.42	0.73
35	2.78	2.56	0.76	3.09	2.57	0.77	3.41	2.8	0.79	3.52	3.03	0.79	3.73	3.02	0.8	3.94	3.21	0.81
40	2.35	2.28	0.71	2.62	2.29	0.72	2.88	2.49	0.73	2.97	2.70	0.74	3.15	2.68	0.74	3.33	2.87	0.75
46	2.16	2.11	0.71	2.41	2.12	0.72	2.66	2.31	0.74	2.74	2.5	0.74	2.9	2.49	0.74	3.07	2.65	0.75